Influenza A virus dissemination and infection leads to tissue resident cell injury and dysfunction in viral sepsis

Ying Zheng,[a,b,l] Di He,[a,b,l] Wenting Zuo,[b,c,l] Weiyang Wang,[b,c,l] Kaiwei Wu,[b,c] Hongping Wu,[b] Yingying Yuan,[d] Yijiao Huang,[b,e] Hongyan Li,[f] Yameng Lu,[a] Ling Zhao,[g] Xiuhong Wang,[g] Jiaying Wang,[h] Yulian Zhang,[i] Guming Zou,[j] Haibo Li,[b,k,***] Zai Wang,[b,d,f,**] and Bin Cao[a,b,c,e,k,*]

[a]Department of Pulmonary and Critical Care Medicine, China-Japan Friendship Hospital, Capital Medical University, Beijing, 100054, China
[b]National Center for Respiratory Medicine, State Key Laboratory of Respiratory Health and Multimorbidity, National Clinical Research Center for Respiratory Diseases, Institute of Respiratory Medicine, Chinese Academy of Medical Sciences, Department of Pulmonary and Critical Care Medicine, Center of Respiratory Medicine, China-Japan Friendship Hospital, Beijing, 100029, China
[c]Peking Union Medical College, Chinese Academy of Medical Sciences, Beijing, 100730, China
[d]Peking University China-Japan Friendship School of Clinical Medicine, Beijing, 100083, China
[e]Tsinghua University-Peking University Joint Center for Life Sciences, Beijing, 100084, China
[f]Institute of Clinical Medical Sciences, China-Japan Friendship Hospital, Beijing, 100029, China
[g]Department of Pathology, China-Japan Friendship Hospital, Beijing, 100029, China
[h]College of Integrated Chinese and Western Medicine, Hebei Medical University, Shijiazhuang, 050017, Hebei, China
[i]Department of Neurosurgery, China-Japan Friendship Hospital, Beijing, 100029, China
[j]Department of Nephrology, China-Japan Friendship Hospital, Beijing, 100029, China
[k]New Cornerstone Science Laboratory, Department of Pulmonary and Critical Care Medicine, Center of Respiratory Medicine, China-Japan Friendship Hospital, Beijing, 100029, China

eBioMedicine
2025;116: 105738
Published Online 13 May 2025
https://doi.org/10.1016/j.ebiom.2025.105738

Summary

Background Severe respiratory viral infections can lead to viral sepsis (VS), a life-threatening condition characterized by lung and extrapulmonary organ dysfunction. However, the pathology of VS is not clear. Specifically, it is unknown how the cytokine storm and direct virus infection contribute to the damage of extrapulmonary organs.

Methods In this study, we established survival and lethal mouse models of VS by intranasally administering different doses of PR8/H1N1 influenza virus in C57BL/6J male mice, as well as model of bacterial sepsis (BS) caused by *Streptococcus pneumoniae* as references. Viraemia and extrapulmonary dissemination and infection of the virus were examined. Single-cell sequencing of the lungs and livers was performed at different days post-infection (dpi) in three groups.

Findings While bacteria can spread and colonize extensively in extrapulmonary organs, causing multiple organ injuries, IAVs mainly replicate and cause damage in pulmonary cells. Live virus can be isolated in the blood and extrapulmonary organs. Disseminating via the bloodstream, IAVs transiently infect the liver and spleen, causing liver dysfunction and spleen atrophy, without affecting kidney function, despite systematically elevated cytokine levels. Compared to BS, a more significant decrease in the proportion of alveolar macrophages, epithelial cells, endothelial cells, and fibroblasts in the lungs, as well as endothelial cells and Kupffer cells in the liver, was observed in VS. This was accompanied by a longer activated PANoptosis pathway and downregulated genes responsible for barrier function and antigen presentation in the epithelial and endothelial cells.

Interpretation Our study suggests that H1N1 influenza virus disseminates through the bloodstream and infects extrapulmonary organs to varying extents, which may lead to differential cell death, organ dysfunction, and trigger VS.

Funding This research was supported by the National Natural Science Foundation of China (82241056, 82170015, 82030002, 82470007, 824B2001), the National Key R&D Program of China (2023YFC2306300), Chinese Academy of

*Corresponding author. National Center for Respiratory Medicine, State Key Laboratory of Respiratory Health and Multimorbidity, National Clinical Research Center for Respiratory Diseases, Institute of Respiratory Medicine, Chinese Academy of Medical Sciences, Beijing Key Laboratory of Surveillance, Early Warning and Pathogen Research on Emerging Infectious Diseases, Department of Pulmonary and Critical Care Medicine, Center of Respiratory Medicine, China-Japan Friendship Hospital, Beijing, 100029, China.
**Corresponding author. Institute of Clinical Medical Sciences, China-Japan Friendship Hospital, Beijing, 100029, China.
***Corresponding author. National Center for Respiratory Medicine, State Key Laboratory of Respiratory Health and Multimorbidity, National Clinical Research Center for Respiratory Diseases, Institute of Respiratory Medicine, Chinese Academy of Medical Sciences, Beijing Key Laboratory of Surveillance, Early Warning and Pathogen Research on Emerging Infectious Diseases, Department of Pulmonary and Critical Care Medicine, Center of Respiratory Medicine, China-Japan Friendship Hospital, Beijing, 100029, China.
E-mail addresses: caobin_ben@163.com (B. Cao), wzai_163pass@163.com (Z. Wang), shrineswe@vip.qq.com (H. Li).
[l]These authors contributed equally to this work.

Medical Sciences Innovation Fund for Medical Sciences (2021-I2M-1-048), the Innovation Team and Talents Cultivation Program of National Administration of Traditional Chinese Medicine (ZYYCXTD-D-202208), New Cornerstone Science Foundation, National High Level Hospital Clinical Research Funding (2024-NHLHCRF-LX-01-0101, 2024-NHLHCRF-LX-01-0102), Beijing Research Ward Excellence Program (BRWEP2024W114060103), Noncommunicable Chronic Diseases-National Science and Technology Major Project (2023ZD0506200, 2023ZD0506203) and Special Research Fund for Central Universities, Peking Union Medical College (3332024193).

Keywords: Respiratory viral sepsis; Bacterial sepsis; Pneumonia; Influenza virus; *Streptococcus pneumoniae*

Research in context

Evidence before this study

Previous clinical reports have shown that, similar to bacterial sepsis, respiratory viruses could be detected in multiple organs and body fluids outside the lungs in severe viral pneumonia, which was associated with poor prognosis. Other studies also showed that respiratory viruses such as PR8/H1N1 influenza virus could spread to and replicate in the hearts of mouse models after pulmonary infection, leading to cardiac dysfunction.

Added value of this study

We established mouse models of viral sepsis (VS) and bacterial sepsis (BS) and employed single-cell RNA sequencing (scRNA-seq) on lung and liver tissues of these models at different days post infection. We demonstrated that live H1N1 influenza virus could directly disseminate through the bloodstream and infect extrapulmonary organs to varying extents, which may be the main cause of organ dysfunction in VS. Additionally, we identified changes of cellular functions in the lungs and livers that may contribute to the spread of the virus and extrapulmonary organ dysfunction in VS.

Implications of all the available evidence

This research provided deeper understanding of the similarities and differences between VS and BS, offering a detailed description of the dynamic changes of viraemia and cellular states in the lungs and livers. This finding may have significant implications for the treatment of VS in clinical practice.

Introduction

Respiratory virus infections caused by respiratory viruses such as the influenza virus (IAV) and SARS-CoV-2 have been significant to threaten human health in this century. These infections not only lead to common cold symptoms, but may also cause dysfunction of lung and extrapulmonary organs, posing a serious risk to the lives of patients.

For IAV, clinical reports have demonstrated that besides pneumonia, it can also lead to damage in other organs, such as the heart, brain, kidneys, liver, muscles, eyes, and blood systems. The most prevalent complications are viral myocarditis, viral encephalitis[1] and liver injury. The extent of extrapulmonary dysfunction caused by different viral strains varies. Highly pathogenic avian influenza viruses (HPAIV), including H7N9 and H5N1, often lead to multi-organ infections and severe disease.[2] Pandemic influenza viruses, such as the 2009 pandemic strain, can cause complications like myocarditis,[3,4] liver damage,[4,5] and kidney injury.[6] Seasonal influenza viruses may also lead to extrapulmonary complications, particularly in populations with underlying chronic conditions.[7] In a human challenge experiment, 4 (26·6%) out of 15 subjects infected by the H1N1 influenza virus experienced a significant increase in ALT.[8] During the 2009 influenza pandemic, elevated liver enzymes were observed more frequently.[5]

For SARS-CoV-2, it can cause dyspnoea, cardiovascular disease, liver failure, kidney failure, and coagulation dysfunctions in patients.[9] These patients met the diagnostic criteria for sepsis or septic shock according to the Sepsis-3 International Consensus.[10] Our previous study showed that 59% of adult hospitalized patients infected with the original strain developed sepsis, and 48% among them died.[11]

Therefore, after the outbreak of COVID-19, we call attention to this multiple organ dysfunction caused by the dysregulated host response against the respiratory viral infection, namely viral sepsis (VS).[12,13] In clinical settings, the diagnosis of sepsis can be indicated by a SOFA score≥ 2,[10] and VS was defined as sepsis resulted from viral pneumonia.[14] However, the unclear pathological mechanism underlying VS greatly hampers the development of effective intervention therapies. Although specific antiviral drugs have been developed for SARS-CoV-2 and influenza in recent years, there remains a lack of drugs for other respiratory viruses. Furthermore, there is a severe shortage of immunomodulatory drugs that target the host. While glucocorticoids and immunomodulatory drugs are available for severe COVID-19, antibiotics, fluid replacement, and vasoactive agents remain the most commonly used treatments for both BS and VS. For IAV-induced severe

cases, no immunomodulatory drugs are available and glucocorticoids are not recommended.[12,15] Therefore, it is imperative to determine whether the pathological mechanism of VS differs from BS, which may lead to effective drug development.

The cytokine storm, considered as an important trigger to bacterial sepsis (BS),[16] was also important for VS. In viral sepsis caused by respiratory viruses such as IAV or SARS-CoV-2, cytokine storms or systematically elevated cytokine levels have been reported to be associated with disease severity and mortality.[17–19] However, it has been found that while bacterial sepsis typically causes severe damage to multiple organs, respiratory viral infections usually result in more severe lung damage but less severe damage to other organs outside the lungs.[20,21] In addition, it is evident that the extent of extrapulmonary organ damage may not be consistent under the same level of cytokine exposure, as various levels of cardiovascular, neurological, urological, and hepatic dysfunctions are recorded in different patients.[22,23] Therefore, other factors besides cytokine storm could be considered for causing this differential extrapulmonary injury.

In our previous studies, we have found a correlation between viral nucleic acidaemia and poor prognosis,[15,24] which raises doubts about whether the virus can spread to multiple organs through the bloodstream and cause damage. There have long been occasional reports of live viraemia in severe influenza infections.[25,26] Additionally, SARS-CoV-2 and influenza viruses have been detected in multiple organs of autopsy biopsies and even live virus can be isolated.[27,28] Therefore, we hypothesized that respiratory viruses primarily infect the lungs and cause significant damage. After spreading through the bloodstream, the virus may also infect other organs to a lesser extent, potentially causing varying degrees of damage.

In this study, we established mouse models of survival and lethal VS through intranasal instillation of different doses of the PR8/H1N1 influenza virus, as well as model for bacterial sepsis caused by *Streptococcus pneumoniae* (Spn), which is the most common pathogens causing community-acquired pneumonia. We evaluated the spread of the virus through the blood stream and the resulting damage to extrapulmonary organs in the VS groups. We then utilized single-cell transcriptome sequencing technology to analyse cell proportions and gene expression in the lungs and liver at various time points after infection, attempting to elucidate the distinct cellular and molecular mechanisms underlying lung and extrapulmonary injury in VS compared to BS.

Methods

Virus and bacteria

The H1N1 influenza A virus (IAV) PR8 strain (A/Puerto Rico/8/1934) (ATCC, Cat# VR-95), influenza A virus (A/WS/1933 (H1N1)) (ATCC, Cat# VR-1520) and influenza A virus (A/Wisconsin/67/2005 (H3N2)) (ATCC, Cat# VR-1881) were obtained from ATCC. The virus was amplified in chicken embryos. Briefly, 100 plaque-forming units (PFU) virus in 100 μL DPBS was injected into the 9- to 11-day-old embryonated chicken egg above the air sack. The pin hole in the shell was sealed with melted candle wax. The egg was incubated at 37 °C for 2 days, and then transferred to 4 °C for at least 12 h. The allantoic fluid was collected into a 15 mL conical tube. The supernatant containing the virus was obtained by centrifugation at 3000 g for 10 min at 4 °C. The viral titre was measured using a plaque assay in the Madin–Darby canine kidney (MDCK) (ATCC, Cat# CCL-34) cell line and 2 μg/mL TPCK-treated trypsin (Thermo Fisher Scientific, Cat# 20233) was added. Briefly, a monolayer of MDCK cells was inoculated in a 12-well plate, and infectious samples were subjected to a tenfold serial dilution with serum-free DMEM, starting from the undiluted stock solution. Cells were washed twice with PBS and infected with 100 μL dilution for 1 h at 37 °C. Gently rock plates every 20 min, after which a solid overlay comprising DMEM medium, 2% agarose, and 2 μg/mL TPCK-treated trypsin was added. After 48 h of infection, cells stained with 0·2% crystal violet and plaques were counted.

The high virulent Spn strain TH870 (type 6 A) was kindly provided by Dr. Jing-Ren Zhang at Tsinghua University, Beijing, China. Pneumococci were cultured in Todd-Hewitt broth with 0·5% yeast extract or tryptic soy agar plates with 3% defibrinated sheep blood at 37 °C with 5% CO_2 as described.[29]

Ethics

The Animal Ethics Committee of Beijing Laboratory Animal Research Center Co. Ltd (BLARC-JSB-DW/013-JL/001) and Institute of Biophysics, Chinese Academy of Sciences (No. ABSL-2-2023019) reviewed and approved all animal experiments, which were performed according to the Principles of Laboratory Animal Care.

Animal experiments

This study was conducted in compliance with the ARRIVEreporting guidelines.[30] Specific pathogen-free C57BL/6 J male mice (8–10 weeks old) weighing 20–25 g were purchased from Vital River Laboratory Animal Technology Co., Ltd, Beijing, China. Mice were held five per cage under specific-pathogen-free conditions with food and water ad libitum. The feeding conditions were as follows: 24 ± 2 °C; 50 ± 10% relative humidity; 12-h light/dark cycle. Mice were acclimatized to the laboratory conditions for 5–7 days prior to experimentation.

The individual mouse was considered the experimental unit within the study. The sample size was guided by our experimental design and reflected consideration of ethical principles and adherence to the 3Rs (Replacement, Reduction, and Refinement) in animal use. At least three replicates were set for molecular and immunofluorescence experiments. At least five

replicates were set for other experiments. The following are the numbers of animals used in different experiments. Body weight and survival rate (n = 40); cytokines analysis and H&E staining (n = 80); biochemical analysis and blood routine examination (n = 147); viral RNA analysis in organs (n = 21); plaque assay for live virus (n = 20); viraemia (n = 25); siNC or siGNE tranfected animal experiments (n = 26); intravenous injection models (n = 45); scSeq (n = 54); flow cytometry (n = 20); PI and NP staining (n = 18); barrier function and neutralizing antibodies assay (n = 20); spleen weight (n = 9); viral RNA in parenchymal cells (n = 5); bacterial loads (n = 8). A total of 538 units were used in this study.

Healthy male mice (8–10 weeks old) weighing 20–25 g were included in the study; those not meeting these criteria were excluded. Samples that were outside the detection range in cytokine analysis and biochemical and blood routine examination were excluded.

For this study, experimental units were randomly assigned to groups according to the ear marker number of mice. Briefly, mice were tagged with ear markers prior to the experiment and the simple random sampling method was used to assign the ear marker numbers into groups for the experiment. The control group was always processed first to avoid cross-contamination between different groups, therefore investigators who conducted experiments could not be blinded. Investigators who evaluated H&E staining results were unaware of the group allocations. The location of mouse cages was randomized. In a multi-time-point experiment, the time of collecting samples was consistent each day.

To establish VS or BS models, the mice were anesthetized with an intraperitoneal injection of 1% pentobarbital sodium (45 mg/kg), and then intranasally inoculated with 10^5 or 10^3 PFU PR8 virus in 30 μL PBS for the VS models, or 2×10^6 colony forming units (CFU) TH870 Spn in 30 μL PBS for the BS model or 10^4 PFU influenza A virus (A/WS/1933 (H1N1)), and 3×10^6 PFU influenza A virus (A/Wisconsin/67/2005 (H3N2)) in 30 μL PBS for the comparison. 30 μL PBS was intranasally inoculated in control group. Mice were monitored daily and euthanized if their weight loss exceeded 30% of the initial body mass or if they met other endpoint criteria, such as severe hunching posture and lack of mobility according to previous studies.[31]

To establish a tail vein injection model, the mice were intravenously injected with 10^6 PFU and 10^4 PFU PR8 in 200 μL saline solution, respectively. 200 μL saline solution was intravenously injected in control group. Blood, lungs, hearts, kidneys, livers, and spleens were harvested at 5 min, 2 h, 24 h, and 72 h.

To detect dead cells in the mice, propidium iodide (1 mg/kg) (MedChemExpress, Cat# 00-4976-93) was injected into mice via the tail vein 1 h before harvest.

To establish a severe acute respiratory distress syndrome (ARDS) mouse model, the mice were intratracheally injected with LPS derived from *Escherichia coli* (O111:B4) (15 mg/kg) (Sigma–Aldrich, Cat# 93572-42-0) in 30 μL PBS, and the blood samples were collected for analysis 3 days post injection. 30 μL PBS was intratracheally injected in control group.

Blood samples were collected from the heart. For blood routine examination, 200 μL of anticoagulant blood was used. Another 300 μL serum was used for biochemical analysis, including lactate dehydrogenase (LDH), creatine kinase (CK), creatine kinase MB (CK-MB), aspartate aminotransferase (AST), alanine transaminase (ALT), total bilirubin (TBill), creatinine (CREA), and urea nitrogen (BUN). The tests were performed by Beijing Yiming Fuxing Biotechnology Co. Ltd, China and the Institute of Clinical Medical Sciences in China–Japan Friendship Hospital.

Multiple cytokine analysis

To quantify the production of cytokines or chemokines in the animals at different time points after infection, serum IL-1α, IL-1β, IL-2, IL-3, IL-4, IL-5, IL-6, IL-9, IL-10, IL-12 (p40), IL-12 (p70), IL-13, IL-17A, Eotaxin, G-CSF, GM-CSF, IFN-γ, KC, MCP-1 (MCAF), MIP-1α, MIP-1β, RANTES, TNF-α were measured using Bio-Plex Pro Mouse Cytokine 23-plex Assay panel and the Bio-Plex 200 system (Bio-Rad, Cat# M60009RDPD, Hercules, CA, USA) according to the manufacturer's instructions.

Histological analysis

For histological analysis, the tissue samples were fixed in neutral formalin overnight, and then prepared into paraffin sections for H&E staining.

For immunofluorescence, the tissues samples were fixed in neutral formalin for 2 h, balanced in 30% sucrose/PBS overnight, and then prepared into frozen sections before staining. Immunofluorescent staining was performed according to the standard procedure.

The primary antibodies used were: anti-nucleocapsid protein (Sino Biological, Cat# 11675-T62, RRID: AB_3676512), anti-NP (Santa Cruz Biotechnology, Cat# sc-101352, RRID: AB_1124491), anti-*S. pneumoniae* (abcam, Cat# ab20429, RRID: AB_445576). The secondary antibodies used were Alex Fluor® 488 Goat Anti-Mouse IgG (H + L) (abcam, Cat# ab150113, RRID: AB_2576208), Alex Fluor® 488 Donkey Anti-Rabbit IgG (H + L) (Thermo Fisher Scientific, Cat# A-21206, RRID: AB_2535792), Alex Fluor® 555 Donkey Anti-Rat IgG (H + L) (Thermo Fisher Scientific, Cat# A48270, RRID: AB_2896336), and Alex Fluor® 555 Donkey Anti-Mouse IgG (H + L) (Thermo Fisher Scientific, Cat# A-31570, RRID: AB_2536180). DAPI (Yeasen, Cat# 40728ES03, Shanghai, China) was used to stain the cell nuclei.

Isolation of the virus from mouse blood and extrapulmonary organs

Blood samples were collected in EDTA tubes. Centrifuge the blood sample at 200×*g* for 10 min at 4 °C. After centrifugation, three distinct layers will be visible:

platelet-poor plasma (PPP) (top), Platelet-rich plasma (PRP) (middle), and haemocytes (bottom). Plasma was isolated from the upper layer. PRP was collected from the middle layer. Next, the PRP was transferred into a new tube and centrifuged at 500×*g* for 10 min to pellet the platelets. Haemocytes were isolated from the bottom layer. Then, platelet and haemocytes pellet were resuspended in PBS. The separated PPP, platelet, and haemocytes from the peripheral blood were collected at 2 and 3 dpi to isolate the virus. About 100 μL of PPP, platelet, and haemocytes were injected into the 9- to 11-day-old SPF embryonated chicken eggs as previously described. The allantoic fluid was harvested and tested using an HA assay. Then the virus isolation rate of different parts of whole blood can be calculated. The virus isolation from the whole blood and tissue homogenates was similar to the virus isolation procedure above. Briefly, whole blood and fresh tissue samples including hearts, livers, and kidneys were collected in 1·5 mL tubes. 200 μL whole blood was injected into SPF embryonated chicken eggs. 500 μL sterile PBS was added to the tubes and then the tissues were cut using sterile scissors and homogenized using a tissue homogenizer. The tubes were centrifuged at 500×*g* for 10 min at 4 °C to obtain supernatant. Then, 500 μL supernatant was totally injected into SPF embryonated chicken eggs. The allantoic fluid was harvested and tested using a plaque assay.

RNA extraction and PCR analysis

The RNA of tissue samples was extracted by TRIzol reagent (Invitrogen, Cat# 15596018CN, Waltham, MA, USA) and plasma samples were extracted using QIAamp viral RNA mini kit (QIAGEN, Cat# 52904, Hilden, Germany) according to the manufacturer's instructions for virus detection. The HifairIII 1st Strand cDNA Synthesis kit (Yeasen, Cat# 11141ES60, Shanghai, China) was used for reverse transcription and the PowerUp SYBR Green Master Mix (Thermo Fisher Scientific, Cat# A25742, USA) for real-time fluorescent quantitative PCR detection. Briefly, approximately 0·1 mg fresh tissue of samples were collected in 1·5 mL tubes. 500 μL of TRIzol reagent was added and then the tissues were homogenized and total RNA was extracted. 1 μg of RNA was reverse-transcribed into cDNA, and 10 ng of cDNA was used for the qRT-PCR reaction. The primers for qRT-PCR were listed in Supplementary Table S1 (Table S1). In experiments for detecting viral NP RNA load in tissues, viral load was calculated by plotting Ct values onto the standard curve based on the standard product of plasmid containing NP sequence. In experiments for detecting relative expression of RNA load, Gapdh was used as an internal control.

Barrier permeability assessment

The integrity of the lung barrier was evaluated using the Evans blue dye extravasation technique (Sigma–Aldrich, Cat# 314-13-6, St. Louis, MO, USA). Mice were intravenously administered 100 μL of 1% Evans blue dye. Thirty minutes post-injection, cardiac perfusion was conducted, followed by the retrieval of lung tissues.

CFU quantification

Blood samples collected from Spn-infected and control mice were processed to obtain platelet-free plasma via centrifugation at 3000 rpm for 5 min. Subsequently, lung, heart, liver, and kidney tissues were harvested and weighed. Tissue samples were homogenized using 3 mm diameter steel beads (Servicebio, Cat# G0103-200G, Wuhan, China) in PBS with a homogenizer (HUXI, Shanghai, China), followed by serial dilution with ten times. The diluted homogenates and plasma were spread on 5% sheep blood agar plate and incubated at 37 °C with 5% CO_2 for 12 h. The Spn colonies were then counted and presented as 1og10 (CFU)/0·1 g of tissue.

Preparation of single-cell suspensions

To obtain the single-cell suspension, lungs, livers, and kidneys were trimmed of fat and connective tissue, then finely minced using scissors. The resulting fragments were incubated and digested for 30 min at 37 °C in 5% CO_2 using the Mouse Lung Dissociation Kit (Miltenyi Biotech, 130-095-927), Mouse Liver Dissociation Kit (Miltenyi Biotech, 130-105-807), and kidney digestion medium (a gift from Beijing SeekGene BioSciences Co., Ltd.), respectively, following the manufacturers' instructions. Digestion was terminated by adding an equal volume of PBS. The cell suspensions were then filtered through a 70 μm cell strainer and collected by centrifugation at 400×*g* for 5 min. Erythrocytes were subsequently removed by incubating the samples with RBC lysis buffer (Solarbio, R1010) at room temperature for 10 min. Finally, the cells were collected again by centrifugation at 400×*g* for 5 min.

Flow cytometry

For flow cytometry, single-cell suspension of lungs was first stained with LIVE/DEAD ™ Fixable Near IR (876) Viability kit for 808 nm excitation (ThermoFisher Scientific, 2841589) in PBS at room temperature in the dark for 30 min. After replacing PBS with Staining Buffer (biolegend, 420201), CD16/CD32 blocking (biolegend, anti-mouse CD16/32 antibody, 101320) was conducted at room temperature in the dark for 30 min. Cells were then stained with respective antibodies at room temperature in the dark for 30 min. All the cells were fixed prior to flow cytometry (ThermoFisher Scientific, 00-8222-49). Flow cytometric analysis was performed using a CytoFLEX LX flow cytometer (Beckman Coulter), and the resulting data were analysed using Cytexpert software (Beckman Coulter, version 2·5·0·77). The information of antibody was listed in Supplementary Table S2 (Table S2).

siRNA knockdown

Mouse liver cell line AML-12 (Procell, Cat# CL-0602, China) was used to test the knockdown efficiency. The sequences of siRNAs were listed in Supplementary Table S3 (Table S3). 110 pmol siNC, siGNE_1, siGNE_2 were transfected into AML-12 cells in 6-well plate by mixing with 8 μL siRNA-mate (GenePharma, Cat# G04026, China) in 200 μL opti-MEM. After incubating for 5 min at room temperature, the mixture was added to the culture medium. RNA was extracted from the cells 48 h after transfection. qRT-PCR was performed using primers in Supplementary Table S1 (Table S1).

To test the knockdown of Gne on the infection efficiency in vitro, AML-12 were seeded in 96-well plates. 24 h later, the cells were transfected with individual siRNAs, and then infected with PR8 at MOI = 1 48 h after transfection. Cells were collected to measure viral RNA expression level by qRT-PCR 24 h after infection.

To test the knockdown of Gne on the infection efficiency in vivo, 40 μg GNA + GalNac modified siNC or siGNE_2 were mixed with 30 μL invivo-siRNA mate (GenePharma, Cat# G04031, China) and 140 μL buffer. The mixture was injected into the tail vein of the mice. 24 h later, the mice were challenged with 10^5 PFU PR8 virus. The livers of the mice were harvested at 3 days post infection, digested into single cells and subjected to qRT-PCR to detect the expression levels of Gne and viral NP genes. The sera of the mice were harvested at 5 days post infection to perform the biochemical analysis.

Neutralization assays

Fifteen mice were randomly divided into three treatment groups, each consisting of five mice: (1) PBS control group; (2) PR8 infection group with 10^3 PFU; (3) PR8 infection group with 10^5 PFU. Plasma samples were collected five days post-infection. MDCK cells were seeded in 96-well plates at a density of 3×10^4 cells per well in complete DMEM. Serial 2-fold dilutions of the plasma samples were prepared in serum-free DMEM containing 2 μg/mL TPCK-treated trypsin. The PR8 virus stock was diluted to achieve a multiplicity of infection (MOI) of 0·1 and mixed with an equal volume of diluted plasma, followed by a 30-min incubation at room temperature to allow neutralization. The serum-virus mixtures were then added to MDCK cells and incubated for 2 h at 37 °C. Then the culture medium was replaced with serum-free DMEM to remove unbound viruses, and the cells were incubated for an additional 3 days at 37 °C. Infectivity was identified by the presence of CPE.[32] The titre was calculated as the highest plasma dilution that eliminated virus CPE in 50% wells per dilution.

Single-cell transcriptome sequencing of lung and liver samples

For isolation of single cells from the lungs, lung tissues from three mice were removed and placed in storage medium (Miltenyi Biotech, Bergisch Gladbach, Germany) until further processing. Three lung samples from mice with the same treatment conditions were mixed together and used as one sample. Lung lobes were minced with scissors and mixed. About 1/3 volume of total lung tissues were digested in enzymatic digestion medium (Miltenyi Biotech, Bergisch Gladbach, Germany) for 30 min at 37 °C. Cell suspensions were pressed through 70 μm cell strainers. Red blood cells were lysed in 1 mL Red Blood Cell Removal Solution (Miltenyi Biotech, Bergisch Gladbach, Germany) for 10 min at 4 °C, washed with 10 mL wash buffer (1 × PBS, 0·04% BSA, 0·01 mM EDTA) and resuspended in wash buffer to generate a cell suspension with a concentration of 700–1200 cells/μL.

Liver samples were collected from the VS and BS groups at 3 and 7 dpi, as well as the PBS control group, for snRNA seq analysis. Three liver samples from mice with the same treatment conditions were mixed together and used as one sample. Approximately 500 mg of liver tissue was dissociated into a single-cell nucleus suspension using tissue homogenization in a cold lysis buffer (Termo Scientific, Cat# O0381, USA), filtered through a 70 μm cell strainer, and mixed with an equal volume of 50% iodixanol solution (0·16 M sucrose, 10 mM NaCl, 3 mM $MgCl_2$, 10 mM Tris HCl pH 7·4, 1U/μL RiboLock RNase inhibitor, 1 mM DTT, and 0·1 mM PMSF protease inhibitor) (Thermo Scientific, Cat# 36978, USA) to achieve a final concentration of 25%. 1 mL of 33% iodixanol solution was added at the bottom of the 50 mL centrifuge tube and 30% iodixanol solution at the top. The solution was mixed 10 times in reverse and then centrifuged at 500×*g* for 8 min at 4 °C. The myelin layer was then removed from the top layer. The cell nuclei were collected from the interface of the 30% iodixanol, resuspended in nuclear washing and resuspension buffer (0·04% bovine serum albumin, 0·2 U/μL RiboLock RNase inhibitor, 500 mM mannitol, and 0·1 mM PMSF protease inhibitor in PBS), and centrifuged at 500×*g* and 4 °C for 5 min. The sample was filtered through a 40 μm cell filter, and the cell numbers were counted with a fluorescent hematocytometer. The nuclear concentration was adjusted to 700–1200 nuclei/μL and examined using a 10 × chromium platform.

Barcoded full-length cDNAs were generated by reverse transcribing polyadenylated mRNA. Silane magnetic beads were then employed to remove any remaining biochemical reagents and primers after the GEM reaction. Then cDNA libraries were constructed and sequenced using the Chromium Next GEM Single Cell 3′ Reagent Kits v3·1 on a Novaseq 6000 platform (Illumina, SD, USA).

Analysis of single-cell RNA-sequencing data of lung samples

The raw sequencing data were first demultiplexed and then aligned to the reference genome mm10-1·2·0 using

the Cell Ranger v3·1·0 pipeline by 10 × Genomics. After this step, the gene expression matrix was converted into Seurat objects using the Seurat (v4·3·0) R package. Influenza genome (NCBI records: NC-002016·1, NC-002017·1, NC-002018·1, NC-002019·1, NC-002020·1, NC-002021·1, NC-002022·1, NC-002023·1) was set as a joint reference.[33] Low-quality cells were filtered out which had less than 200 genes expressed, genes detected in fewer than 3 cells and more than 10% mitochondrial-derived genes. Next, we evaluated and sorted the doublets using Scrublet,[34] and these doublets were identified manually in cell type annotation by specific markers, and removed. Then the obtained 164,584 cells matrices were normalized, scaled, and processed by using principal component analysis (PCA) as tutorials. We further visualized the data and these clusters were plotted by using uniform manifold approximation and projection (UMAP).

After the first-round of unsupervised clustering (the resolution was set to 1·0), *Ptprc*, *Pdgfrb*, *Pecam1* and *Epcam* were used to cluster all cells into immune cells, mesenchymal cells, endothelial cells and epithelial cells. Then these major clusters underwent the same dimensionality reduction, clustering, visualization as described above and batch correction using Harmony algorithm[35] and further were clustered into subgroups and manually annotated by individual cell markers (Supplementary Table S4).

Differentially expressed gene (DEG) analysis was performed using the 'FindMarkers' function in Seurat. Then, the Kyoto Encyclopedia of Genes and Genomes (KEGG) pathways were analysed utilizing the enrichKEGG functions in the R package ClusterProfiler (v4·6·2),[36] and pvalueCutoff was set to 0·05. Furthermore, gene set variation analysis (GSVA) was employed to score the pathway activity in each sample based on Hallmarks gene sets.

Hallmarks gene sets and other gene sets used in this study were obtained from the Molecular Signatures Database (MSigDB). We also created a Viral gene set including eight viral gene segments of PR8 to evaluate the distribution of viral genes in individual cells. Then we calculated the signature score of specific gene sets, including Inflammatory response, IFN-γ response, IFN-α response, Coagulation, Complement, Apoptosis, Necroptosis and Pyroptosis scores in different cell types using AddModuleScore function in Seurat. We then fit each score to the time in different groups using a polynomial regression model (the highest degree was set to 2) as previous studies.[37]

The definition of "viral load" in a cell is the percentage of UMIs mapped to one of eight viral segments in the total mapped UMIs. Viral load was classified into four categories: none (<0·05%), low (between 0·05% and 0·5%), medium (between 0·5% and 5%), and high (>5%). These definitions were used in previous studies.[33,38]

Analysis of single-cell RNA-sequencing data of liver samples

For the newly generated scRNA-seq data, Cell Ranger (v3·1·0, 10 × Genomics Inc) was used for sequencing reads mapping against mm10-1·2·0 mouse reference genome, UMI counting and cell identification. Then, we applied Seurat (v5·0·1) to convert gene expression matrix into Seurat objects. Genes detected in ≥1 cells were kept, cells with more than 200 and less than 10000 genes detected or <25% mitochondrial UMI counts were kept. We followed the suggested workflow described in the author's tutorial pages and used the R package DoubletFinder (v2·0·4)[39] to remove potential doublets from each sequencing library. The expected doublet rate was set to 0·076, and cells identified as doublets were filtered out using default parameters.

Then, the D0_ctrl, D3_V2, D7_V2, D3_B, and D7_B matrices were normalized, scaled, and subjected to principal component analysis (PCA) based on the highly variable genes identified. Gene–cell count matrices from different samples were merged using Canonical Correlation Analysis (CCA) as the integration method. The resulting combined matrix, comprising 74,837 cells, was prepared for downstream analysis. We constructed nearest neighbour graphs using the 'FindNeighbors' function and applied the Louvain algorithm for clustering with a resolution of 0·8 using the 'FindClusters' function. Dimensionality reduction was performed using UMAP.

We used the FindMarkers and FindAllMarkers functions to identify DEGs, applying Bonferroni correction with adjusted $P < 0·05$. Manual annotation was performed using canonical cell markers derived from previously published studies. Epithelial cells, including hepatocytes and cholangiocytes, were collectively analysed in the cluster analysis.

Developmental pseudotime was determined using the Monocle package (version 2·28·0). First, raw counts were converted from the Seurat object into a CellDataSet object using the importCDS function. Next, ordering genes were selected with the differentialGeneTest function (FDR-adjusted P-value <0·01), identifying genes likely to be informative for cell ordering along the pseudotime trajectory. Dimensionality reduction and clustering analysis were performed using the reduceDimension function, followed by trajectory inference with the orderCells function, both using default parameters.

Statistical analysis

Statistical analyses were performed using GraphPad Prism software (version 10·1·2). The one-way analysis of variance (ANOVA) followed by Dunnett's multiple comparison test was used to compare the values of the treated groups against the control group. The one-way ANOVA followed by Tukey's post hoc test was employed to compare values among multiple treated groups.

Unpaired t test was used to compare values between two groups. The values are presented as means ± SD for the indicated sample sizes. P-values < 0·05 were considered statistically significant.

Role of funders

The funders were not involved in any aspect of the study, including its design, data collection, analysis, interpretation, report writing, or the decision to publish.

Results

Establishment of models for respiratory viral sepsis and bacterial sepsis

To establish VS models, we used intranasal inoculation of the IAV PR8 strain with doses of 10^5 and 10^3 PFU. While all mice in the 10^5 PFU group died by the 8th day, no mouse in the 10^3 PFU group died, thus generating a VS lethal group and a VS survival group. In parallel, we used intranasal inoculation of 2×10^6 CFU Spn TH870 to model BS, resulting in a mortality rate of approximately 70% while avoiding very early death (Fig. 1a and b and Supplementary Fig. S1a).

Inflammatory cytokine storms are considered to play important roles in both VS and BS. We detected inflammatory factors in the serum at multiple time points in the three groups. As a result, cytokines including TNFα, IFNγ, IL-1β, IL-6, IL-17A, IL-10, MIP-1α, GM-CSF, IL-12 (P70) were upregulated during the acute phase in the three groups, with differences in the dynamic trends observed. In the VS lethal group, the cytokines gradually increased along the time, with most reaching peak levels in 5–7 days post infection of the acute phase, which is higher than that in the VS survival group. In the BS group, IL-1β, IL-6, and IL-10 upregulated dramatically, which are higher than those in the VS groups. For the difference between VS survival and VS lethal groups, we found that IL-6 was more upregulated since 2 dpi to 7 dpi in VS lethal than in VS survival group, which may serve as a biomarker to discriminate these two groups (Fig. 1c).

To evaluate multiorgan damage, we conducted blood routine tests and blood biochemical tests on these modelled mice. The results showed a decrease in both the absolute values and percentages of lymphocytes, while an increase was observed in both the absolute values and percentages of neutrophils in both the VS and BS groups (Supplementary Fig. S1b). ALT level significantly increased in both the VS and BS groups, suggesting liver dysfunction in both models. However, LDH, CK, and CK-MB, which indicate cardiac function, as well as UREA and CREA, which indicate renal function, showed elevated levels in the BS group, while remaining constant in the VS groups (Fig. 1d and Supplementary Fig. S1c). The results in the VS groups are unexpected, as the systematic increase of the cytokines did not lead to uniform organ damage.

Histopathology analysis confirmed severe bronchopneumonia in both the VS and BS groups, with visible bleeding, oedema, and extensive infiltration of inflammatory cells in the lungs. While the formation of bacterial colonization foci could be observed in the heart and kidney, and significant tissue necrotic damage could be observed in the liver of mice in the BS group, the pathological damage to extrapulmonary organs in the VS group was not as obvious as that in the BS group, with only small focal necrosis observed in the liver (Fig. 1e), and spleen atrophy was evident at 5 dpi in the VS lethal group (Supplementary Fig. S1d).

Dispersion of the virus to extrapulmonary organs through bloodstream

Since increased levels of cytokines alone cannot explain the differential organ damage in the VS groups, we suspect that the dissemination and infection of the pathogen in the extrapulmonary organs, rather than the cytokine storm, might be the primary reason for the organ dysfunction. We first test this hypothesis in the bacteria infection model. We established a severe acute respiratory distress syndrome (ARDS) mouse model by intratracheal injection of LPS and monitored their biochemical values prior to death. The rationale behind this model is that when LPS is injected intraperitoneally to induce sepsis, it disperses throughout the body, mimicking a bacterial infection in multiple organs. Previous studies have shown clear evidence of multi-organ damage in this scenario.[40] However, in our LPS intratracheal injection model, the LPS remains mainly in the lungs and does not significantly harm the extrapulmonary organs. As expected, unlike the LPS intraperitoneal injection model, the LPS intratracheal injection only caused slight impairment of the liver and kidney as shown by biochemical abnormalities, suggesting that direct bacterial infection, rather than a cytokine storm, is the primary cause of extrapulmonary organ injury in BS (Supplementary Fig. S1e).

Similar to bacterial infection, since the increased levels of cytokines alone cannot explain the differential organ damage in the VS groups, we suspected whether there was differential viral infection occurring in these extrapulmonary organs. We discovered that the viral RNA was detectable in the heart, liver, spleen, kidney and brain in the VSL group (Fig. 2a), indicating that the virus can spread to these organs.

Besides PR8, we also used the H1N1(WS) and H3N2 strains to infect the mice. As a result, H1N1(WS) caused an elevation in liver and kidney functional indicators, while H3N2 did not show significant changes in the indicator levels (Supplementary Fig. S2a–d). Meanwhile, the plaque assay results also confirmed the presence of infectious virus particles in the heart, liver and kidneys of PR8-induced VS models, as well as in these organs in H1N1(WS)-infected mice, but only in the heart of H3N2-infected mice (Fig. 2b).

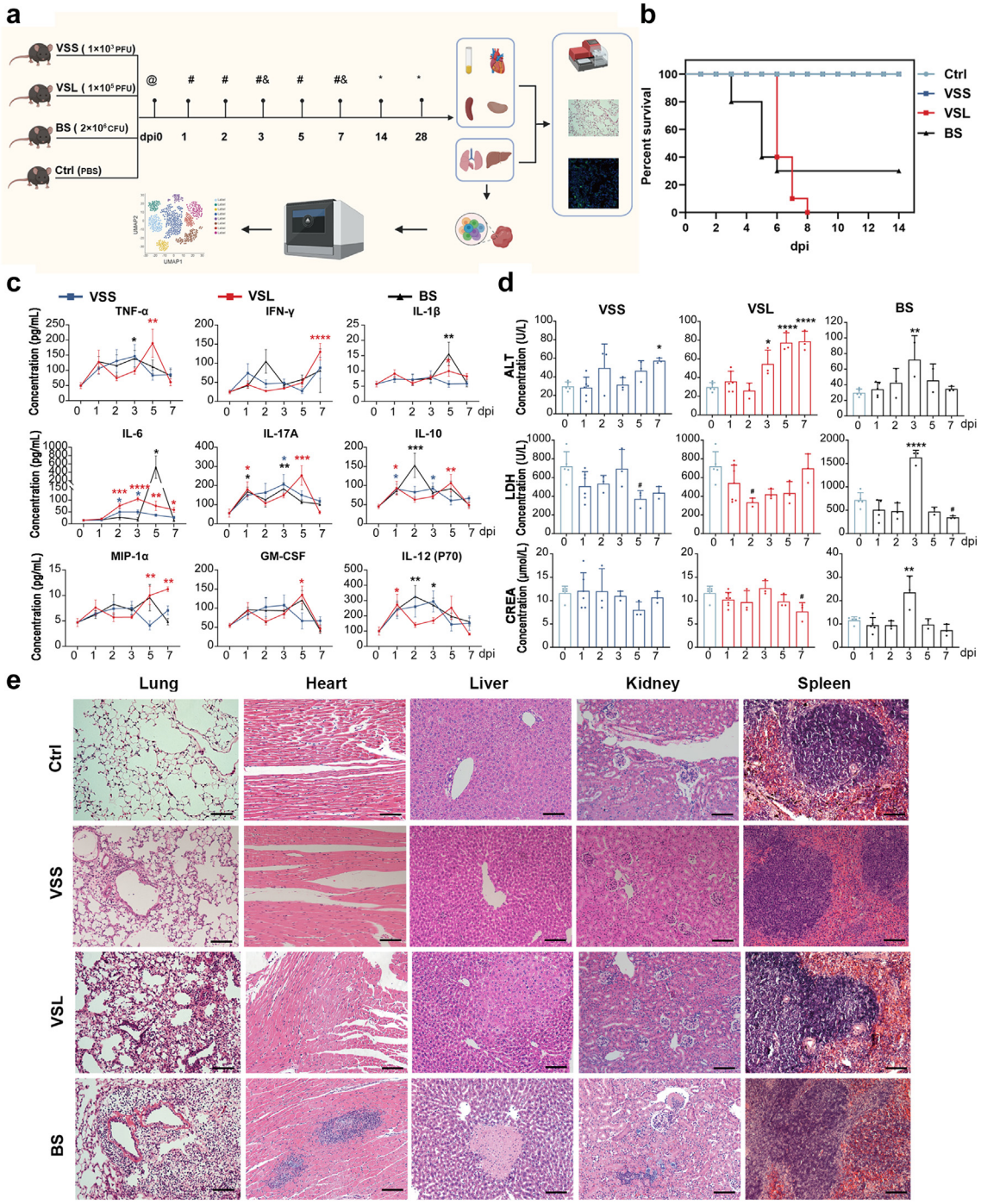

***Fig. 1:* Establishment of mouse models of VS survival (VSS), VS lethal (VSL), and BS.** (a) Schematic diagram of animal model preparation and experimental design. 1 × 10^3 PFU PR8, 1 × 10^5 PFU PR8, and 2 × 10^6 CFU Spn were intranasally administrated to establish the VSS, VSL, and BS mouse models, respectively. @ Ctrl group. # The lung tissues were harvested from three animals for each group at 1, 2, 3, 5, 7 dpi and control group and mixed for scSeq. * Additional three lung tissues from VSS group were obtained at 14 and 28 dpi. & the liver tissues were harvested from three animals for VSL and BS group at 3 and 7 dpi and control group and mixed for snSeq. Created with BioRender.com. (b) Survival rate of Ctrl, VSS, VSL, and BS mouse models (n = 10). (c) Serum levels of cytokines at 0, 1, 2, 3, 5, 7 dpi as indicated. The values are presented as means ± SD for the indicated sample sizes. Comparisons were analysed by one-way ANOVA with Dunnett's multiple comparison test. (d) Results of blood biochemical tests of the VSS, VSL, and BS groups at 0, 1, 2, 3, 5, 7 dpi as indicated (n = 3–7). The values are presented as means ± SD for the indicated sample sizes. Comparisons were analysed by one-way ANOVA with Dunnett's multiple comparison test. *, #, P < 0·05, **, ##, P < 0·01, ***, ###, P < 0·001, ****P < 0·0001. (e) H&E staining on the paraffin sections of lung, heart, liver, kidney, and spleen of the Ctrl, VSS, VSL and BS groups at 0 and 7 dpi. Scale bar: 100 μm.

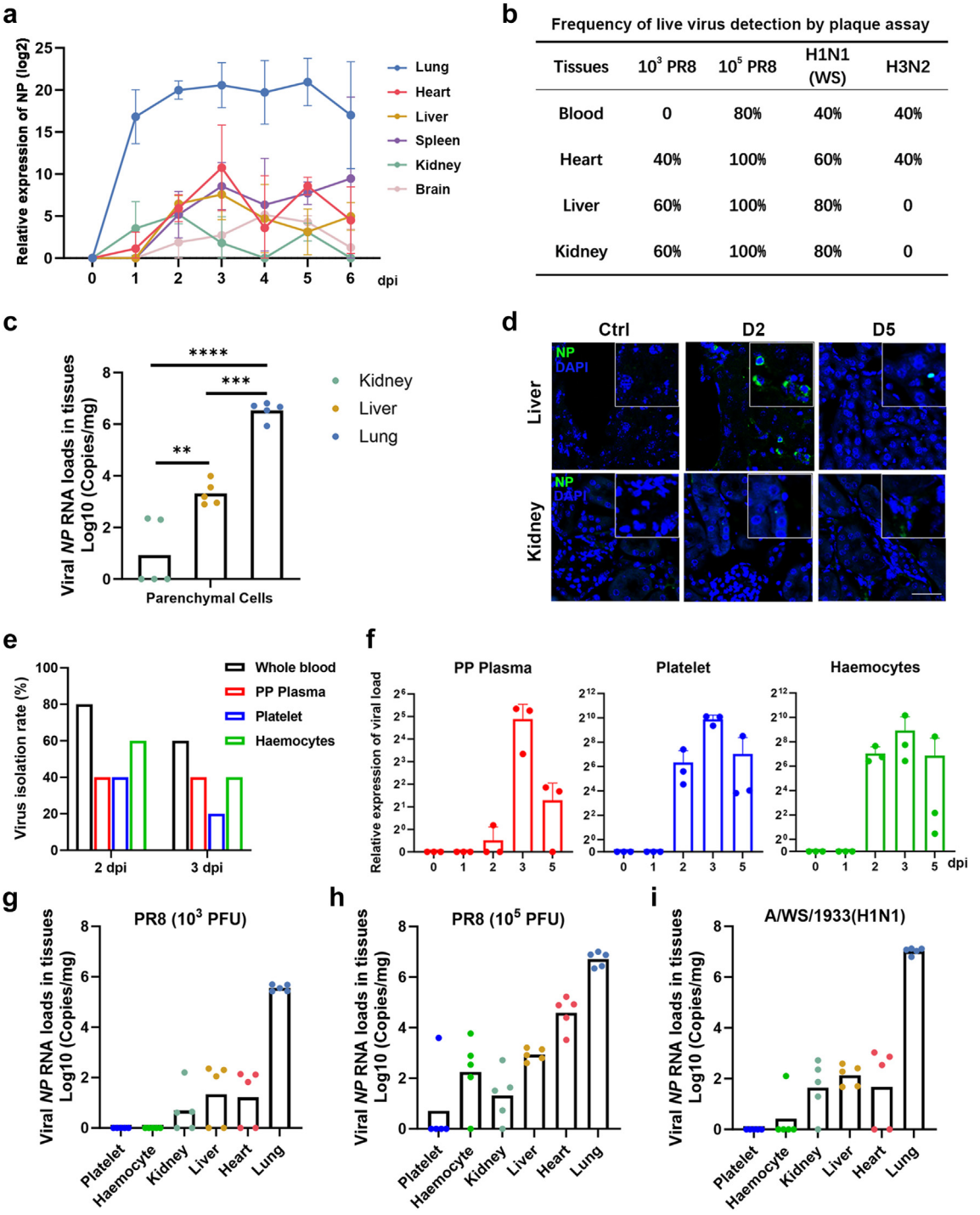

***Fig. 2:* Virus dispersion to the extrapulmonary organs**. (a) Detection of viral RNA in the lung, heart, liver, spleen, kidney and brain from the VSL group by qRT-PCR. Gapdh was used as an internal control (n = 3). The values are presented as means ± SD for the indicated sample sizes. (b) Frequency of detection of live virus by plaque assay from different tissues of mice infected with different virus strains at 3 dpi (n = 5). The limit of plaque assay is 1 PFU. (c) Detection of viral RNA in parenchymal cells of different tissues in VSL group at 3 dpi. (n = 5). Data points represent individual value. Comparisons were analysed by one-way ANOVA with followed by Tukey's post hoc test.*, #, P < 0·05, **, ##, P < 0·01, ***, ###, P < 0·001, ****P < 0·0001. (d) Immunofluorescence of IAV NP expression in the kidney and liver at 0, 2, 5 dpi. Scale bar: 20 μm. (e) Virus isolation rate in the separated platelet-poor plasma (PPP), platelet, and haemocytes from the peripheral blood at 2 and 3 dpi (n = 5). (f) Detection of viral RNA in the separated PPP, platelet, and haemocytes from the peripheral blood at 0, 1, 2, 3 and 5 dpi as indicated (n = 3). The values are presented as means ± SD for the indicated sample sizes (g–i) Detection of viral RNA in different tissues in mice infected with 10^3 PFU PR8 (g), 10^5 PFU PR8 (h), and H1N1(WS) (i) at 3 dpi (n = 5).

To investigate whether the virus exists in the organs that can truly infect host cells in extrapulmonary organs, we digested the kidney and liver into single cells, removed the interstitial tissue that may include the disseminated virus, and performed qRT-PCR analysis. The results showed that the number of virus genes detected in liver cells was significantly higher than in kidney cells, indicating a higher level of viral infection in liver cells (Fig. 2c). Immunofluorescence analysis confirmed strong expression of the viral NP protein in the lung at 5 dpi and weak expression in the liver at 2 dpi, but no NP protein expression was detected in the kidney either at 2 or 5 dpi (Fig. 2d, Supplementary Fig. S3a). The Spn protein was detected dispersedly in the lung and liver, and in clusters in the heart and kidney at 3 dpi (Supplementary Fig. S3a). This finding is consistent with the previously measured functional damage in these organs, suggesting that, similar to bacteria, the virus may spread to extrapulmonary organs and cause varying degrees of damage based on different levels of infection.

To further verify the role of virus infection in liver damage, we knocked down the expression of GNE, a rate-limiting enzyme, UDP-GlcNAc 2-epimerase/ManNAc kinase, involved in sialic acid synthesis in the mouse liver,[41,42] to limit viral infection in this organ, as sialic acid serves as a receptor for IAV entry.[43] We chose this gene because hepatic conditional knockout of this gene did not affect liver function according to the literature,[44] and downregulation of sialic acid on the surface of the cells may inhibit IAV infection.[45] We first select siGNE_2, as this siRNA showed more than 80% knockdown efficiency (Supplementary Fig. S3b) and 50% reduction of viral gene expression in the mouse liver cell line AML-12 (Supplementary Fig. S3c). As a result, in vivo injection of GNA + GalNac modified siRNA downregulated *Gne* and viral *NP* gene expression at 3 dpi (Supplementary Fig. S3d, e), and the liver functional indicators AST and ALT showed a decreasing trend at 5 dpi compared to the control (Supplementary Fig. S3f, g), indicating that virus infection may play a role in compromising liver function.

Since the virus is most likely to spread through the bloodstream, we conducted various experiments to isolate mouse plasma at different time points after infection, including virus amplification in chicken embryos, and plaque assays. Our findings indicate that live viruses can be isolated from the whole blood in both the PR8-induced VS lethal group and the H1N1 (WS) group at 3 days post-infection (dpi) (Fig. 2b, Supplementary Fig. S3h). Furthermore, we separated platelet-poor plasma (PPP), platelets, and haemocytes from the peripheral blood and discovered that live virus can be found in all three components at 2 and 3 dpi (Fig. 2e). Additionally, the viral RNA levels were highest at 3 dpi in these three blood components (Fig. 2f). The quantity of live virus, as well as the amount of viral RNA, depends on the viral dose in the lungs and the specific viral strain (Fig. 2g–i). Notably, it is more likely to detect viruses in extrapulmonary organs than in blood (Fig. 2b, g–i), suggesting that even if viruses are not detected in the blood, it cannot be ruled out that there may be live viruses in the extrapulmonary organs. The reason may be that there are a large number of immune cells in the blood, which have a strong ability to clear the viruses. In comparison, extrapulmonary organs may provide a better habitat for the viruses. Together, all these data suggest that the influenza virus in the lungs may penetrate the gas-blood barrier and enter the bloodstream, subsequently spreading to extrapulmonary organs through the serum or by utilizing platelets or haemocytes as a means of transportation.

To visualize the consequences of viraemia directly, we conducted a tail vein injection model by injecting 10^4 or 10^6 PFU PR8. We observed that within 5 min after injection, the virus primarily accumulated in blood cells and lungs. After 2 h, the viral load in peripheral blood and lungs notably decreased. Interestingly, at 24 h post-injection, the viral load in organs such as the lungs, liver, and spleen increased, indicating successful invasion and replication of the uneliminated virus in these organs. However, after 72 h, the viral load in the liver and spleen significantly decreased, which may be caused by quickly elimination of virus by immune response or abortive infection of the virus in these organs. Permissive replication of the virus only occurred in a portion of the lungs in the 10^6 group, as the viral load continued to increase (Supplementary Fig. S3i, j). The residence and proliferation of viruses in the lungs were confirmed by immunofluorescence (Supplementary Fig. S3k). As a control, live Spn could be isolated from the lungs, livers, hearts, kidneys, and blood (Supplementary Fig. S3l, m).

Monocyte-derived macrophage recruitment at early stage and T cell proliferation at late stage in the lungs are prominent features in VS

To investigate the distinct cellular and molecular mechanisms of VS in more detail, we conducted single-cell transcriptome sequencing on the lungs at 1, 2, 3, 5, and 7 dpi for all three groups. We categorized the cells in the lungs into 21 distinct populations (Fig. 3a; Supplementary Table S4), and observed significant changes in cell composition across the three groups.

One noteworthy change in the BS group was the infiltration of neutrophils, which began as early as 1 dpi. The proportion of neutrophils increased from approximately 25% to as high as 60–70% by 3 dpi. There was also an increase in neutrophils in the VS groups. However, in the VS survival group, the proportion of neutrophils returned to normal by 7 dpi. This suggests that the reduced proportion of neutrophils could potentially serve as a biomarker for predicting a favourable prognosis (Fig. 3b).

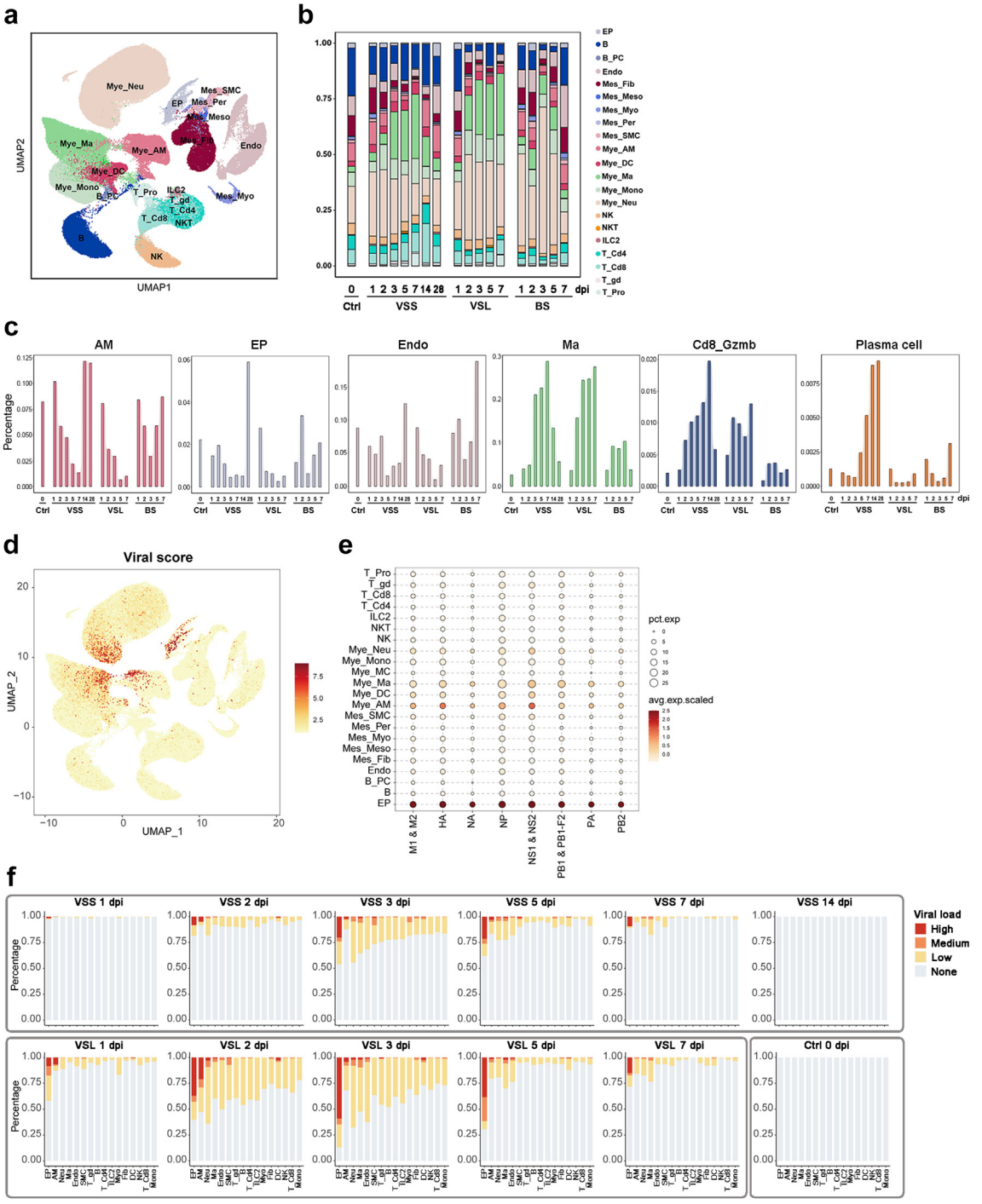

Fig. 3: **Monocyte-derived macrophages recruit to the lungs in the VS**. (a) Dimensionality reduction and clustering of cells in the lung. 21 cell clusters demonstrated by UMAP plot of combined single cell sequencing results of pulmonary cells at different time points post infection in Ctrl, VSS, VSL, and BS groups. (b) Proportion of cell subpopulations at various time points after infection as shown by stacking diagram. (c) Frequencies of AM, EP, Endo, Ma, $CD8^+$ $CZMB^+$T cell and plasma cell in Ctrl, VSS, VSL, and BS groups at the indicated time points. (d) Expression of influenza A virus genes on the UMAP embedding. (e) Expression of different viral gene segments of influenza A virus in clusters as shown by dot plot. (f) Heterogeneity of intracellular viral load in different cell types of lungs in control and virus infected mice. The percentages of viral load are displayed for different cell types, categorized as none (blue), low (yellow), medium (light red), and high (red).

The most significant increase in the proportion of monocyte-derived macrophages was observed in the VS groups. In the control group, this population accounted for less than 5%, but in the VS lethal group, it emerged at 2 dpi, and in the VS survival group, it emerged at 3 dpi. In both groups, it accounted for approximately 30% and remained at this high level until 7 dpi. Conversely, the BS group had significantly fewer monocyte-derived macrophages (Fig. 3b and c).

We found that viral genes are primarily expressed in epithelial cells, followed by alveolar macrophages, as well as in multiple cell types, including neutrophils, monocyte-derived macrophages, endothelial cells, and fibroblasts (Fig. 3d and e). The scSeq results revealed that the viral load peaked at 3 dpi and significantly decreased at 5 and 7 dpi in the VS groups (Fig. 3f). The expression of viral genes aligns with the observed reduction in tissue resident epithelial cells, alveolar macrophages, endothelial cells, and fibroblasts in the VS groups (Fig. 3b and c and Supplementary Fig. S4a–e). We also examined the proportion of cells with viral fragments in different subsets of endothelial cells (Supplementary Table S4). Our analysis revealed that viral RNA was primarily enriched in the endothelial cells of capillary blood vessels; furthermore, it can also be detected in the lymphatic endothelial cells (Supplementary Fig. S4f–h). This finding suggests that, in addition to directly entering the bloodstream through the compromised blood-gas barrier, the virus could also enter the bloodstream via lymphatic reflux.

We then analysed the connection between the proportion of monocyte-derived macrophages and neutrophils and the pulmonary viral load. The decline of viral load aligns with the decline of neutrophils in the VS survival group. However, in the VS lethal group, the decline in neutrophils and monocyte-derived macrophages did not occur until 7 dpi (Fig. 3b, c, f), suggesting that these cells may have potential detrimental functions at the late stage of infection in this group.

For the adaptive immune cells, a decrease in T lymphocytes was observed starting from 3 dpi in all three groups. This decrease was particularly noticeable in $CD4^+$ T cells in the VS lethal and BS groups (Fig. 3b). Interestingly, a population of $Mki67^+$ T cells appeared primarily in the VS groups at 7 dpi (Fig. 3b). In parallel, $GZMB^+$ cytotoxic T lymphocytes significantly increased in the VS groups from 2 dpi (Fig. 3c). The number of B cells decreased in the VS lethal group at 2 and 3 dpi and in the BS group at 3 and 5 dpi (Fig. 3b). Plasma cells increased in the VS survival group at 5 and 7 dpi and increased even more at 14 and 28 dpi while they did not significantly increase in the VS lethal group until 7 dpi (Fig. 3b and c).

Activation of the innate immune response, inflammation and PANoptosis pathways in the lungs in both VS and BS groups

To determine the overall dynamic changes in signalling pathways among three different groups, we conducted an enrichment analysis on hallmark pathways for all cell groups within each group at each time point. All three groups exhibited interferon and inflammatory responses. The BS group displayed the most significant inflammatory response at 3 dpi, and a relatively weaker IFN response at 3 and 5 dpi. In the VS lethal group, the IFN response was higher at 2 dpi, while inflammation was higher at 3 dpi, and they were comparable at 5 and 7 dpi. In the VS survival group, the IFN response was consistently higher than the inflammation response from 2 to 7 dpi (Fig. 4a). We also analysed the above hallmark pathways in different cell types. As a result, interferon response was higher in epithelial cells, endothelial cells, fibroblasts, and alveolar macrophages (Fig. 4b and Supplementary Fig. S5a).

We analysed the functions of monocyte-derived macrophages in the VS lethal group and neutrophils in the BS group. In the VS lethal and survival groups, the significantly recruited monocyte-derived macrophages demonstrated upregulation of pathways related to virus defence (Supplementary Fig. S5b). On the other hand, in the BS group, the neutrophils exhibited upregulation of immunoinflammatory pathways, as well as TNF and NF-kappa B signalling pathways (Supplementary Fig. S5d).

We analysed the upregulated pathways in monocyte-derived macrophages in the VS lethal group by comparing them to the BS group. We observed a stronger upregulation of a panel of virus-induced ISGs, including *Isg15*, *Mx1*, *Rsad2*, *Ifit1*, etc., at 2 and 3 dpi. As the viral load decreased, the expression of these genes also decreased. However, another panel of *Clec7a*/*Mapk*/inflammation-related genes, such as *Clec7a*, *Atf4*, *Jun*, *Junb*, *Fos*, *Fosb*, *Tnf*, and several relative regulators like *Dusp1*, *Gadd45b*, *Gadd45g*, showed sustained or even further upregulation at 5 dpi, indicating a proinflammatory role of monocyte-derived macrophages in VS during the late-acute phase (Fig. 4c and d). We also analysed the pathways between the VS lethal and survival groups. Compared with VS survival group, the inflammation-related pathways of monocyte-derived macrophages at 3 dpi were more significantly elevated in the VS lethal group (Supplementary Fig. S5e).

In the proliferating T cells, in addition to the activation of adaptive immune pathways such as TCR pathways, the PD1-PD-L1 pathways, apoptosis pathways, and NFκB pathways were more activated in the VS lethal group than in the BS group (Supplementary Fig. S5f).

Since the innate immune response of cells can activate the PANoptosis pathway, we examined the expression of death-related genes and assessed the apoptosis, necroptosis, and pyroptosis pathways at different time points after infection in various cell groups in the lungs. These cell groups included epithelial cells, endothelial cells, fibroblasts, and alveolar macrophages, as well as $CD4^+$ T cells, $CD8^+$ T cells, B cells, and plasma cells (Fig. 4e and Supplementary Fig. S6a, b). The extensive

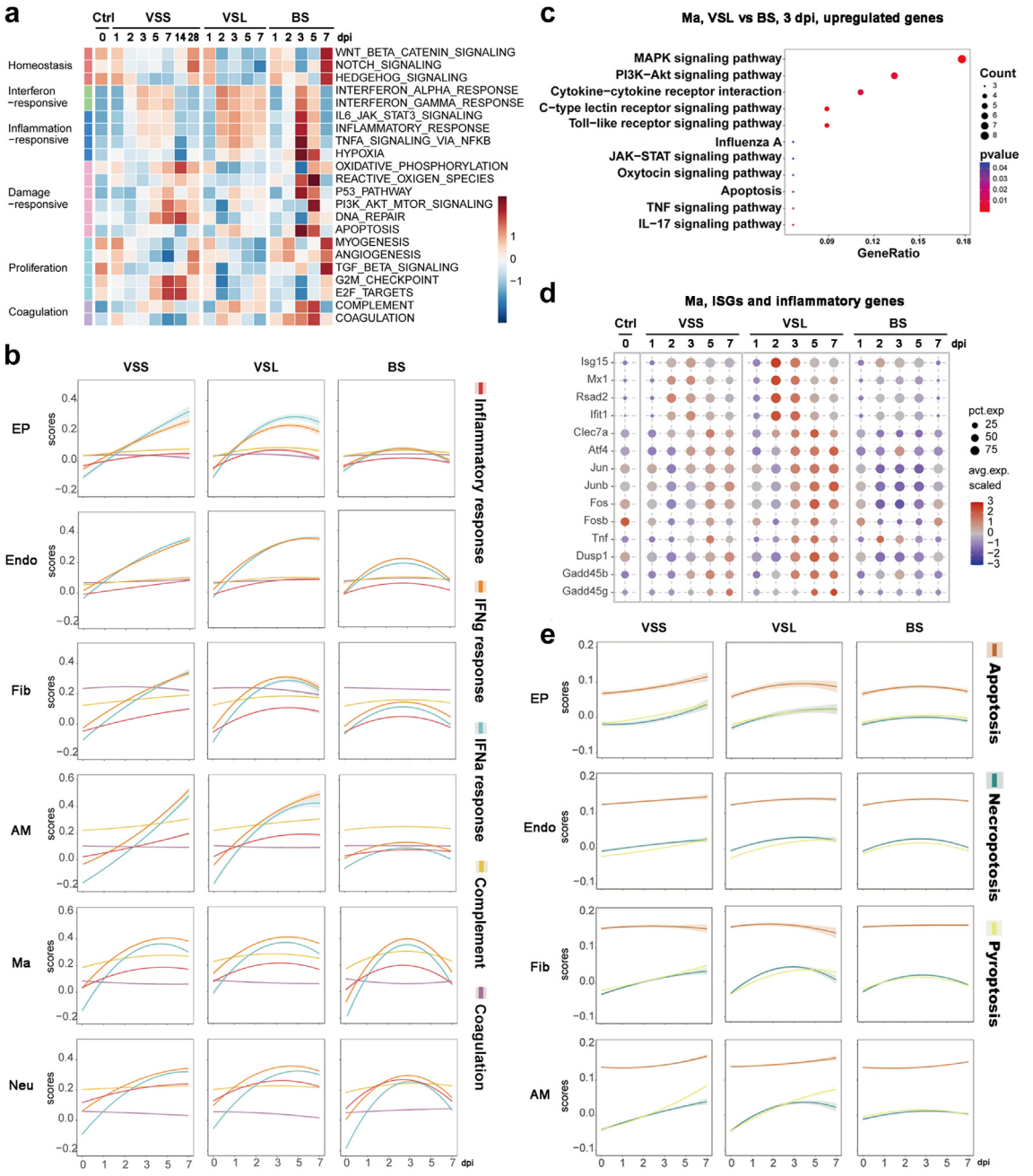

Fig. 4: **Hyperinflammation and PANoptosis coexist in the lungs in VS.** (a) Hallmark enrichment analysis for all cells stratified by samples and groups as shown by heatmap plot. (b) Scores of Inflammatory response, IFN-α response, IFN-γ response, Coagulation and Complement for EP, Endo, Fib, AM, Ma, and Neu plotted along the indicated time points. (c) KEGG pathway enrichment of upregulated genes between VSL and BS in Ma at 3 dpi. The pvalue shown in the figure are unadjusted. (d) Expression of ISGs, inflammatory genes and inflammatory relative regulators in Ma as shown by dot plot. (e) Scores of Apoptosis, Necroptosis and Pyroptosis of EP, Endo, Fib and AM plotted along the indicated time points.

cell death in the lungs was further verified by in vivo propidium iodide staining (Supplementary Fig. S6c). The findings demonstrated that the activated innate immune response could induce PANoptosis in multiple cell types, resulting in cell death.

Barrier functions and surfactant secreting functions are compromised in the lungs in VS

Since pulmonary epithelial and endothelial cells form the blood-air barrier for gas exchange, which is the main function of the lung, we investigated whether the

cellular functions of these two cell types were compromised during viral sepsis. Therefore, we specifically analysed downregulated pathways in the VS lethal group compared to the BS group at 3 dpi. Our findings revealed that cellular junctions and antigen presenting pathways were among the top 30 enriched pathways in both epithelial and endothelial cells (Fig. 5a and b). Furthermore, *Itga1*, *Cav2*, *Cav1*, *Gja4*, *Gja1*, and *Cadm1* exhibited a more significant dysregulation at 3–7 dpi in theVS groups compared to the BS group (Fig. 5c). Compared with the VS survival group, blood-barrier related pathways of EP at 3 dpi in the VS lethal group were more significantly downregulated (Supplementary Fig. S7a). An Evans blue dye extravasation assay was conducted to further confirm the impaired function of blood-air barrier (Supplementary Fig. S7b).

For the antigen presenting genes, *H2-Eb1*, *H2-Aa*, *H2-Ab1*, *H2-DMb1*, and *Cd74*, specific downregulation was observed at 3 or 5 dpi in the VS lethal group within the epithelial cells (Supplementary Fig. S7c). These genes were also examined in DCs and monocyte-derived macrophages, yielding similar results (Supplementary Fig. S7d). To determine whether the potential compromised antigen presentation affected the production of neutralizing antibodies, we analysed the neutralizing antibody levels in the VS groups. As a result, the level of neutralizing antibodies was significantly higher in the VS lethal group than the VS survival group (Supplementary Fig. S7e), suggesting that the production of neutralizing antibodies was not affected in the VS lethal group.

Besides their role in barrier function, epithelial AT2 cells also play an important role in the secretion of surfactant proteins, which is crucial for maintaining pulmonary compliance and preventing the collapse of alveoli at the end of expiration. To investigate this further, we analysed the gene expression related to epithelial secretion. In the VS groups, we observed significant downregulation of genes encoding surfactant proteins A, B, C, and D (*Sftpa*, *Sftpb*, *Sftpc*, *Sftpd*) in the epithelial cells. Additionally, regulatory proteins involved in surfactant metabolism (*Abca3*, *Napsa*,

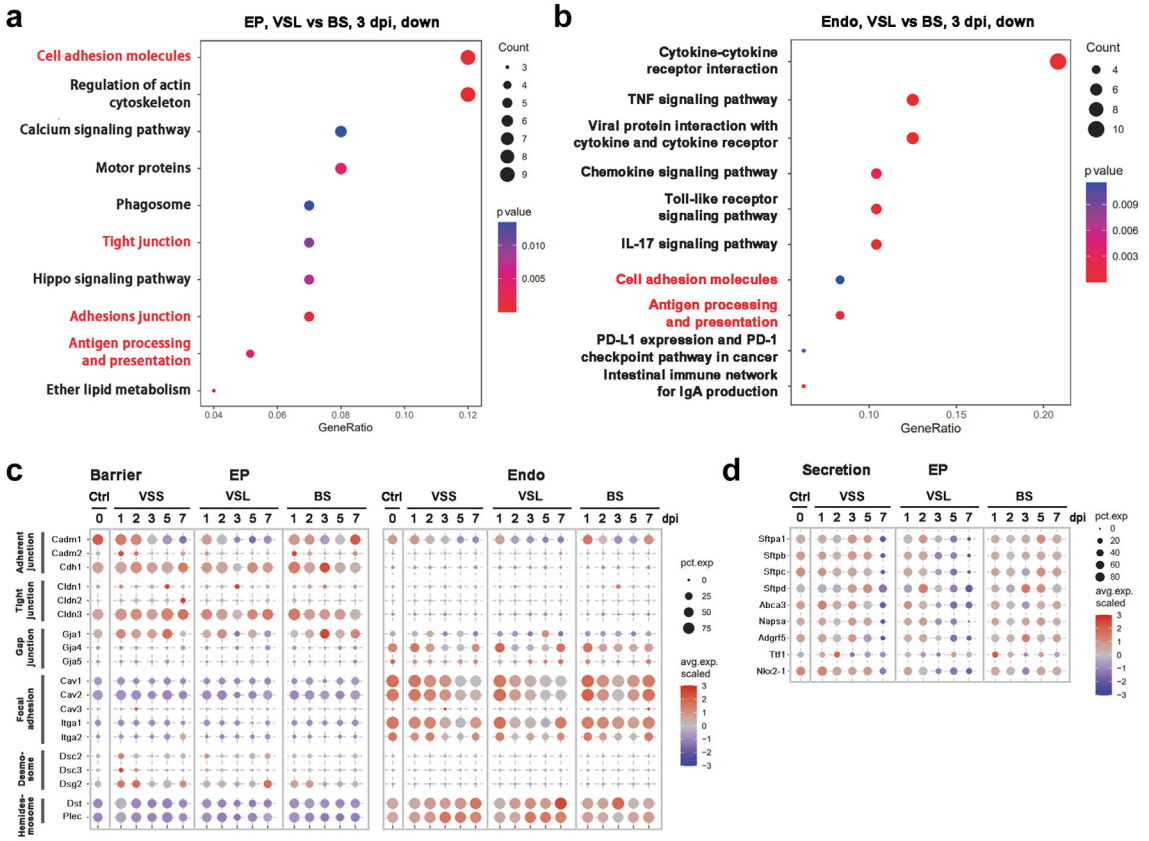

***Fig. 5:* Dysregulated cellular functions in the lungs in VS.** (a & b) KEGG pathway enrichment of downregulated genes between VSL and BS in EP (a) and Endo (b) at 3 dpi. The p values shown in the figure are unadjusted. (c) Expression of cell junction related genes in EP and Endo as shown by dot plot. (d) Expression of genes encoding for surfactant proteins, regulatory proteins of surfactant metabolism and transcription factor in EP as shown by dot plot.

Gpr116, *Ttf1*) and the key transcription factor *Nkx2-1* were also downregulated (Fig. 5d). These findings suggest a compromised function in surfactant protein secretion.

Acute-phase response in hepatocytes and dysregulated cellular functions in cholangiocytes in VS and BS

Since liver function was compromised in both the VS lethal and BS groups according to the data of blood biochemical tests and histopathology analysis, we conducted single-cell transcriptome sequencing of the livers at 3 and 7 dpi in both groups. In total, we classified the cells into 12 populations (Fig. 6a). Among these populations, hepatocytes were further categorized into four sub-populations. This included periportal hepatocytes (Hep_periportal), marked by the expression of glutamate synthetase encoded by Glul; the pericentral hepatocytes (Hep_pericentral), marked by the expression of serine dehydratase encoded by Sds, an important factor in gluconeogenesis; midzone hepatocytes (Hep_mid) with the transcriptome that overlapped with both periportal and pericentral hepatocytes; and acute-phase hepatocytes (Hep_related)[46] characterized as being activated in protein synthesis, mitochondria respiration, and displaying an upregulation of acute phase proteins (Fig. 6b and Supplementary Fig. S8a).

The proportion of total hepatocytes increased gradually at 3 and 7 dpi in both groups, marked by a significant rise in acute-phase hepatocytes, particularly in the VS group. On the other hand, the proportions of the other three subpopulations exhibited a differential decrease. Interestingly, the pericentral and middle zone hepatic cells showed a greater decrease in the VS group, whereas the periportal zone hepatic cells showed a greater decrease in the BS group (Fig. 6c). Pseudotime analysis demonstrates that hepatocytes in all three zones have the ability to transform into acute-phase hepatocytes (Fig. 6d). Therefore, it can be inferred that during the development of VS and BS, liver cells from different zones undergo transformation into acute-phase hepatocytes to defend against pathological challenges.

Additionally, we observed differential changes in the proportion of other cell populations. The endothelial cells, Kupffer cells, and stellate cells decreased more significantly at 7 dpi in the VS group compared to the BS group. On the other hand, the neutrophils and NKT cells increased at 3 dpi only in the BS group, not in the VS group (Fig. 6c).

As mentioned earlier, viral infection of the liver can be a transient event. Therefore, it is not surprising that the viral RNA was not detected in the single-cell sequencing of the liver in the VS group, even though the virus RNA can be detected by PCR (Fig. 2a) and signal of viral NP protein can be observed by immunostaining (Fig. 2d). However, it is worth noting that the interferon response was moderately induced in the hepatocytes in the VS group at 3 dpi and further enhanced at 7 dpi (Fig. 6e), suggesting that the transient liver infection can trigger a delayed interferon response and may have subsequent effects.

In the BS group, there was a significant enhancement in interferon response, inflammatory response, apoptosis, ECM synthesis, and complement pathways in the hepatocytes at 3 dpi, and returned to normal at 7 dpi. These findings are largely consistent with those observed in the lungs (Fig. 6e).

The hallmark pathways analysis of the hepatocytes demonstrated a notable disruption of homoeostasis at 7 dpi in the VS group, characterized by a decrease in bile acid, fatty acid, cholesterol metabolism, and glycolysis. Additionally, we found that the coagulation pathway was upregulated in the VS group at 3 dpi, indicating a potential correlation with the coagulopathy exhibited by patients with viral sepsis. In the BS group, several homoeostatic processes were also disrupted at 3 dpi, indicating a significant disturbance of liver function at this early timepoint. Interestingly, metabolism of haem and xenobiotics was specifically downregulated in the BS group, indicating the acquisition of haem for iron utilization by the bacteria growth,[47] as well as the impact of inflammation on the cytochrome P450 system[48] (Fig. 6e).

Besides hepatic functions, we also investigated the barrier function and bile acid transport function of cholangiocytes in sepsis. Our findings revealed that the expression of the tight junction gene *Cldn1*, which is crucial for bile duct barrier function,[49] was significantly downregulated in the BS group at 3 dpi but recovered by 7 dpi. In contrast, its expression remained significantly downregulated in the VS group from 3 dpi to day 7. For the tight junction proteins, *Tjp1* and *Tjp2* were only significantly downregulated in the VS group and showed no significant change in the BS group (Fig. 6f). Regarding the expression of bile acid transporters,[50] the bile acid transport protein SLC10A2 showed no significant changes in the VS group but decreased in the BS group at 7 dpi. Cftr, on the other hand, was similarly downregulated in both the VS and BS groups, with a greater decrease on day 3 compared to day 7 (Fig. 6g). The expression of Cldn1 and Cftr were also verified by PCR analysis (Supplementary Fig. S8b). These results indicate that both the bile duct barrier function and bile acid transport function may be impaired in both the VS and BS groups.

Discussion

In this study, we established mouse models for influenza VS, and Spn BS, and conducted single-cell transcriptome sequencing at various time points after infection to elucidate the cellular and molecular mechanisms of VS. In the VS model, although the serum levels of cytokines elevated, only elevated levels of liver functional indicators were observed. Consistently, the

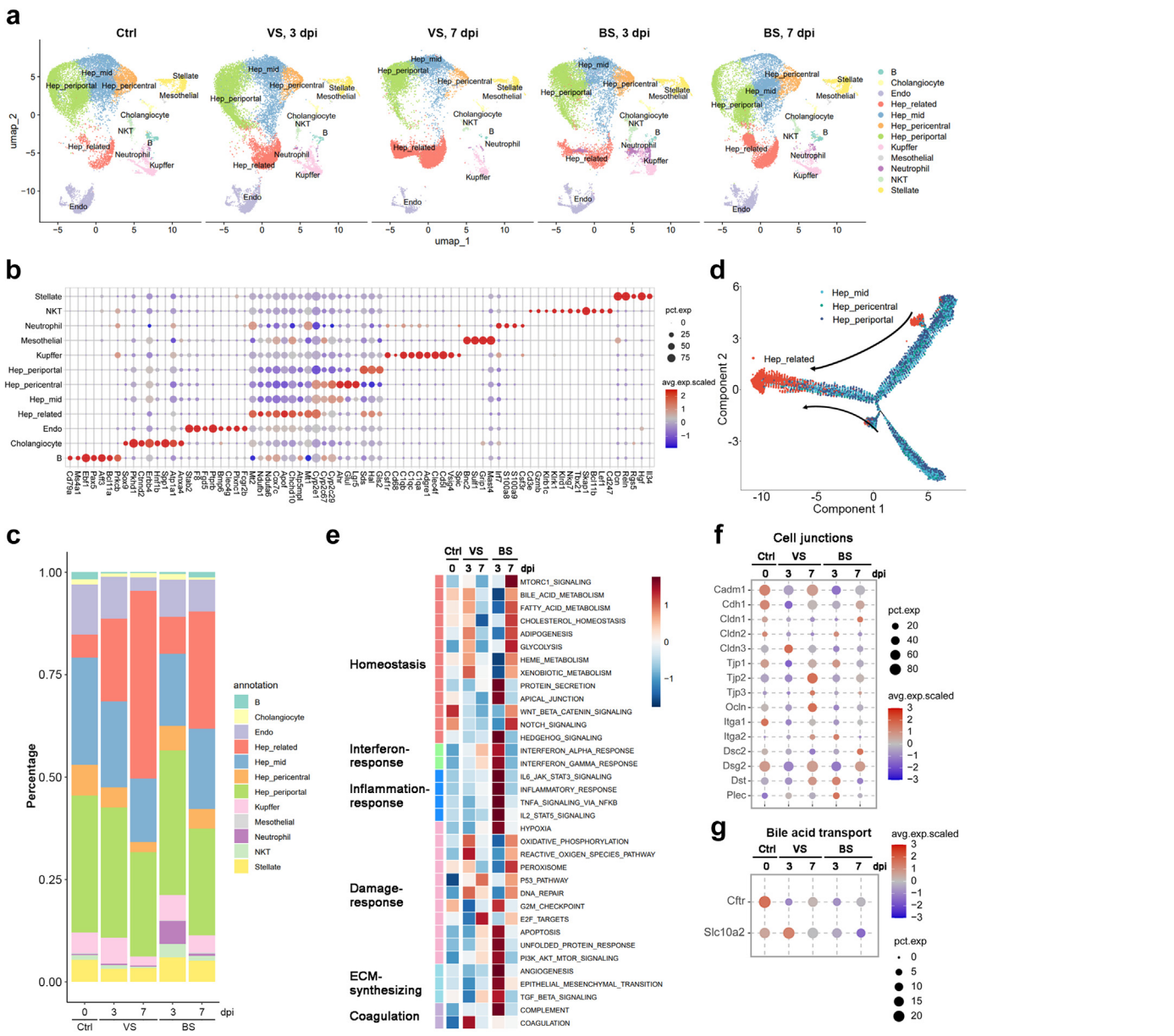

Fig. 6: **Induction of ISGs and dysregulated cellular functions in hepatocytes and cholangiocytes in VS and BS**. (a) 12 cell clusters demonstrated by UMAP plot of combined single cell sequencing results of cells in the livers at 0, 3, and 7 dpi in VS and BS groups. (b) Marker genes expressions in different cell types in the livers as shown by dot plot. (c) Proportion of cell subpopulations at various time points after infection as shown by the stacking diagram. (d) Pseudotime analysis of the differentiation track of hepatocytes subpopulations. (e) Hallmark analysis of the combined hepatocyte subpopulations at 0, 3, and 7 dpi in the VS and BS groups (f & g) Expression of genes of cell junctions (f) and bile acid transportation (g) in cholangiocytes are shown in dot plot.

live influenza virus can spread from the lungs to the extrapulmonary organs via thebloodstream, causing virus infection in the liver. Upon virus infection, the expression of ISGs was induced in the pulmonary cells and hepatocytes, and the expression of genes for cellular functions were downregulated. In this study, we demonstrated that direct viral infection may trigger extrapulmonary organ damage through dysregulated cellular function during VS.

The viraemia and extrapulmonary dissemination of the virus may arouse similarities between the pathology of VS and BS, as bloodstream infection and extrapulmonary implantation is well known in BS. Our previous studies on COVID-19 and adenovirus suggest that respiratory viral nucleic acidaemia is associated with a poor prognosis.[15,24] For influenza, even live viraemia can be detected in severe influenza patients. Virus was isolated most frequently on day 3 after onset of

symptoms. Isolated case reports also indicate that hospitalized patients can exhibit viraemia either pre- or postmortem.[25,26,51,52] In animal models for H7N9 and H5N1, live viruses have been detected in serum and extrapulmonary organs.[53,54] The pandemic influenza might be more likely to cause viraemia and have higher pathogenicity than seasonal influenza.[55] Our study provides a detailed description of the dynamic changes in viral nucleic RNAemia and confirms that live viraemia is most easily detected at 2 and 3 dpi during infection. This suggests that the virus can enter the bloodstream after extensive expansion in the lungs, spread to and infect external organs.

Unlike bacterial sepsis, which occurs when bacteria multiply in large quantities in the blood and cause damage to cells through endotoxins, exotoxins, or bacterial components, viruses are unable to replicate independently in the blood. They mainly cause damage by directly infecting tissue cells. In fact, influenza virus infection can be detected from the extrapulmonary organs, such as in brain, liver, spleen, pancreas, heart, muscle, and kidney.[28,56,57] For viral entry as the first step of infection, the influenza virus prefers to use alpha 2,6-linked sialic acid as an receptor, which is abundant not only in the respiratory systems but also present in placental Hofbauer cells, hepatic bile duct epithelial cells, Kupffer cells, liver cells, glomerular cells, distal tubular cells, splenic B cells, and endothelial cells, etc.[43] This suggests that these cells may also become potential target cells for the influenza virus. However, it remains unclear whether other host factors, such as ectopic trypsins[58] and the endocytic receptor mGluR2,[59] are required for influenza virus entry in various cell types.

For the subsequent steps following viral entry, pulmonary epithelial cells allow for viral replication, packaging, and release of offspring viruses. Some other cell types only support limited replication or abortive infection. In our VS mouse model, although extrapulmonary infection is likely transient, which is consistent with previous report,[60] the viral RNA could be detected at a much higher level in the digested liver cells than in the kidney cells. In addition, viral NP protein can be detected in the liver, but not kidney. The virus infection of the liver cells leads to significant liver function damage.[54] On the other hand, there were no significant changes in renal function indicators. Therefore, the severity of tissue damage may be determined by the degree of viral replication in different organs or the vulnerability of the cell types to virus infection. For the heart, although viral RNA was detected at a similar level as in the liver, no NP protein was detected in the PR8 infection model, and there was no significant change in CK or CK-MB. In the H1N1(WS) strain infection model, CREA elevation was observed. Whether the H1N1(WS) strain has a stronger ability to infect the kidney cells and cause injury requires further investigation. Moreover, there was evidence indicating that targeting virus replication in cardiomyocytes led to the rescue of cardiac dysfunction.[31] Our result also demonstrated that in the mice with sialic acid knockdown in the liver, the viral infection of the liver cells decreased, and the liver functional indicators showed a decreasing trend. These data further confirmed a role of viral infection in the extrapulmonary organ dysfunction.

Nevertheless, the extent of extrapulmonary organ injury differs between animal models and clinical practice. In animal models, liver injury is more pronounced, whereas brain and heart injury are more prevalent in clinical practice. This difference may be attributed to variations in virus strain[61] and host heterogeneity, highlighting the need for further research.

It is known that the virus activates natural immune pathways, leading to PANoptosis of immune cells, such as macrophages[62] and T cells.[63] However, there is limited research on the impact of cell death pathways in the tissue resident cells. Therefore, the purpose of this study is to address these gaps in knowledge. Here we demonstrated that viral infection causes subsequent induction of ISGs and PANoptosis genes not only in immune cells but also in tissue resident cells. In the VS lethal group, where the viral load is higher than in the VS survival group, induction of ISGs and PANoptosis was more prominent in the lungs. Therefore, the proportion of tissue resident epithelial, endothelial, fibroblast cells, and alveolar macrophages decreased more significantly in the VS lethal group.

It is well known that in BS, excessive inflammation and immunosuppression may coexist, leading to a complex dysregulated innate and adaptive immune response, which makes it difficult to restore immune homoeostasis.[64] In our VS lethal model, we inferred that the specific recruitment of monocyte-derived macrophages to the lungs through the activated *Clec7a*/*Mapk*/inflammation axis according to the scRNA-seq data. The overall ISG response and activated inflammation were evident. Furthermore, several antigen presenting genes, including *CD74*, were downregulated in the epithelial cells, monocyte-derived macrophages and DCs, indicating a simultaneous suppression of the immune system in the VS. Additionally, we observed suppressed plasma cell expansion in the VS lethal group in our scRNA-seq data. These findings remind us with reports linking impaired adaptive immune response to severe influenza disease.[64] However, we found that the antibody level was much higher in the VS lethal group than in the VS survival group, indicating that the plasma cell number and function in the lungs may not be associated with the overall antibody response in the body.

In addition to the immune response and cell death, it is also important to pay attention to the changes in cell function in the lungs and other organs during viral infection, since the activation of antiviral immunity may lead to cellular dysfunction. Several single-cell sequencing studies of COVID-19 autopsies have

provided evidence. In the lungs, surfactant genes were downregulated.[65] In the heart, the expression of myocardial structural protein genes is significantly reduced.[66] In the kidneys, genes related to renal function, such as molecular transport and amino acid metabolism, are downregulated.[67] In the liver, the expression of bile duct cell barrier proteins and bile acid transport genes is downregulated.[68] Consistent with these reports, our IAV research shows that in the lungs, the expression of various cell junction proteins in epithelial and endothelial cells is significantly reduced, indicating disruption of the gas-blood barrier. Additionally, genes coding for surfactant proteins and regulatory proteins are also downregulated, indicating impaired surfactant protein secretion of the lung epithelium. In the liver, several epithelial barrier genes and bile acid transport gene *Cftr* of cholangiocytes are downregulated. However, contrary to the results of the COVID-19 study,[68] another bile acid transport molecule, SLC10A2, did not change significantly in the IAV VS group, suggesting that pathogen-specific regulation may play a role.

This study has the following limitations. Firstly, our main conclusions were derived from mice models, which may not be completely applied to human diseases due to variations in virus strain and host heterogeneity. Secondly, there is a lack of mechanistic exploration, such as the mechanisms of barrier damage and how the virus enters the bloodstream, which require further investigation.

Overall, our study clarifies that the influenza virus spreading to organs outside the lungs and infecting target cells may be necessary for causing damage to extrapulmonary function. This finding has significant implications for the treatment of VS. Firstly, it suggests that using antiviral drugs for a sufficient period of time can help limit the spread of the virus and prevent infection beyond the lungs. Secondly, since the dysfunction and loss of tissue resident cells are key distinguishing features of VS as compared to BS, future studies should focus on suppressing PANoptosis signalling and maintaining cellular functions in order to reduce organ damage.

Contributors

BC, ZW, and HBL were involved in conceptualization, methodology, and supervision of the study. YZ, DH, and WTZ were involved in investigation, data curation, and validation. YZ, WYW, and HPW were engaged in analysing data and visualization. KWW, YYY, YJH, HYL, and YML assisted with validating the results. LZ, XHW, JYW, YLZ, and GMZ assisted with data visualization. ZW wrote the original draft, which was revised by all the authors. All authors read and approved the final version of the manuscript.

Data sharing statement

The datasets generated in this study are available in China national center for bioinformation with accession number PRJCA033941. The remaining data are available in the manuscript or in the supplementary materials upon publication of the manuscript or upon request from the corresponding author.

Declaration of interests

The authors declare no competing interests.

Acknowledgements

We thank Prof. Jing-Ren Zhang and Dr. Haoran An (Tsinghua University, Beijing, China) for kindly providing us the important bacteria strains. We thank Prof. Peigang Wang (Capital Medical University, Beijing, China) for his valuable comments on this manuscript. We thank Xinyi Wu (IBP, CAS), Longlong Chen (IBP, CAS), Xin Wen (IBP, CAS) for breeding and management of laboratory animals, excellent animal technical support and experimental data collection services. This work was supported by the National Natural Science Foundation of China (82241056, 82170015, 82030002, 82470007, 824B2001), the National Key R&D Program of China (2023YFC2306300), Chinese Academy of Medical Sciences Innovation Fund for Medical Sciences (2021-I2M-1-048), the Innovation Team and Talents Cultivation Program of National Administration of Traditional Chinese Medicine (ZYYCXTD-D-202208), New Cornerstone Science Foundation, National High Level Hospital Clinical Research Funding (2024-NHLHCRF-LX-01-0101, 2024-NHLHCRF-LX-01-0102), Beijing Research Ward Excellence Program (BRWEP2024W114060103), Noncommunicable Chronic Diseases-National Science and Technology Major Project (2023ZD0506200, 2023ZD0506203) and Special Research Fund for Central Universities, Peking Union Medical College (3332024193).

Appendix A. Supplementary data

Supplementary data related to this article can be found at https://doi.org/10.1016/j.ebiom.2025.105738.

References

1 Sellers SA, Hagan RS, Hayden FG, Fischer WA 2nd. The hidden burden of influenza: a review of the extra-pulmonary complications of influenza infection. *Influenza Other Respir Viruses*. 2017;11(5):372–393.
2 Mostafa A, Abdelwhab EM, Mettenleiter TC, Pleschka S. Zoonotic potential of influenza A viruses: a comprehensive overview. *Viruses*. 2018;10(9).
3 Chacko B, Peter JV, Pichamuthu K, et al. Cardiac manifestations in patients with pandemic (H1N1) 2009 virus infection needing intensive care. *J Crit Care*. 2012;27(1):106.e1–106.e6.
4 Ukimura A, Satomi H, Ooi Y, Kanzaki Y. Myocarditis associated with influenza A H1N1pdm2009. *Influenza Res Treat*. 2012;2012:351979.
5 Papic N, Pangercic A, Vargovic M, Barsic B, Vince A, Kuzman I. Liver involvement during influenza infection: perspective on the 2009 influenza pandemic. *Influenza Other Respir Viruses*. 2012;6(3):e2–e5.
6 Martin-Loeches I, Papiol E, Rodríguez A, et al. Acute kidney injury in critical ill patients affected by influenza A (H1N1) virus infection. *Crit Care*. 2011;15(1):R66.
7 Giacchetta I, Primieri C, Cavalieri R, Domnich A, de Waure C. The burden of seasonal influenza in Italy: a systematic review of influenza-related complications, hospitalizations, and mortality. *Influenza Other Respir Viruses*. 2022;16(2):351–365.
8 Polakos NK, Cornejo JC, Murray DA, et al. Kupffer cell-dependent hepatitis occurs during influenza infection. *Am J Pathol*. 2006;168(4):1169–1178. quiz 404-5.
9 Zhao W, Li H, Li J, Xu B, Xu J. The mechanism of multiple organ dysfunction syndrome in patients with COVID-19. *J Med Virol*. 2022;94(5):1886–1892.
10 Singer M, Deutschman CS, Seymour CW, et al. The third international Consensus definitions for sepsis and septic shock (Sepsis-3). *JAMA*. 2016;315(8):801–810.
11 Zhou F, Yu T, Du R, et al. Clinical course and risk factors for mortality of adult inpatients with COVID-19 in Wuhan, China: a retrospective cohort study. *Lancet*. 2020;395(10229):1054–1062.
12 Gu X, Zhou F, Wang Y, Fan G, Cao B. Respiratory viral sepsis: epidemiology, pathophysiology, diagnosis and treatment. *Eur Respir Rev*. 2020;29(157).
13 Li H, Liu L, Zhang D, et al. SARS-CoV-2 and viral sepsis: observations and hypotheses. *Lancet*. 2020;395(10235):1517–1520.
14 Cao W, Xu J, Liu Z, et al. Poor clinical outcomes in respiratory viral sepsis: a retrospective observational study. *ERJ Open Res*; 2024;00836-2024. https://doi.org/10.1183/23120541.00836-2024.
15 Gu L, Qu J, Sun B, Yu X, Li H, Cao B. Sustained viremia and high viral load in respiratory tract secretions are predictors for death in immunocompetent adults with adenovirus pneumonia. *PLoS One*. 2016;11(8):e0160777.

16 Wiersinga WJ, Leopold SJ, Cranendonk DR, van der Poll T. Host innate immune responses to sepsis. *Virulence*. 2014;5(1):36–44.
17 Hu B, Huang S, Yin L. The cytokine storm and COVID-19. *J Med Virol*. 2021;93(1):250–256.
18 Guo XJ, Thomas PG. New fronts emerge in the influenza cytokine storm. *Semin Immunopathol*. 2017;39(5):541–550.
19 Liu Q, Zhou YH, Yang ZQ. The cytokine storm of severe influenza and development of immunomodulatory therapy. *Cell Mol Immunol*. 2016;13(1):3–10.
20 Ren C, Yao RQ, Ren D, Li Y, Feng YW, Yao YM. Comparison of clinical laboratory tests between bacterial sepsis and SARS-CoV-2-associated viral sepsis. *Mil Med Res*. 2020;7(1):36.
21 Wu M, Zou ZY, Chen YH, Wang CL, Feng YW, Liu ZF. Severe COVID-19-associated sepsis is different from classical sepsis induced by pulmonary infection with carbapenem-resistant klebsiella pneumonia (CrKP). *Chin J Traumatol*. 2022;25(1):17–24.
22 Ning Q, Wu D, Wang X, et al. The mechanism underlying extrapulmonary complications of the coronavirus disease 2019 and its therapeutic implication. *Signal Transduct Target Ther*. 2022;7(1):57.
23 Eisenhut M. Extrapulmonary manifestations of severe respiratory syncytial virus infection–a systematic review. *Crit Care*. 2006;10(4):R107.
24 Li H, Gu X, Li H, et al. Risk factors of viral RNAaemia and its association with clinical prognosis among patients with severe COVID-19. *Chest*. 2021;159(4):1382–1386.
25 Khakpour M, Saidi A, Naficy K. Proved viraemia in Asian influenza (Hong Kong variant) during incubation period. *Br Med J*. 1969;4(5677):208–209.
26 Lehmann NI, Gust ID. Viraemia in influenza. A report of two cases. *Med J Aust*. 1971;2(23):1166–1169.
27 Stein SR, Ramelli SC, Grazioli A, et al. SARS-CoV-2 infection and persistence in the human body and brain at autopsy. *Nature*. 2022;612(7941):758–763.
28 Franková V, Jirásek A, Tůmová B. Type A influenza: postmortem virus isolations from different organs in human lethal cases. *Arch Virol*. 1977;53(3):265–268.
29 Lu L, Ma Y, Zhang JR. Streptococcus pneumoniae recruits complement factor H through the amino terminus of CbpA. *J Biol Chem*. 2006;281(22):15464–15474.
30 Percie du Sert N, Hurst V, Ahluwalia A, et al. The ARRIVE guidelines 2.0: updated guidelines for reporting animal research. *J Cereb Blood Flow Metab*. 2020;40(9):1769–1777.
31 Kenney AD, Aron SL, Gilbert C, et al. Influenza virus replication in cardiomyocytes drives heart dysfunction and fibrosis. *Sci Adv*. 2022;8(19):eabm5371.
32 Lorenzo ME, Hodgson A, Robinson DP, Kaplan JB, Pekosz A, Klein SL. Antibody responses and cross protection against lethal influenza A viruses differ between the sexes in C57BL/6 mice. *Vaccine*. 2011;29(49):9246–9255.
33 Steuerman Y, Cohen M, Peshes-Yaloz N, et al. Dissection of influenza infection in vivo by single-cell RNA sequencing. *Cell Syst*. 2018;6(6):679–691.e4.
34 Wolock SL, Lopez R, Klein AM. Scrublet: Computational identification of cell doublets in single-cell transcriptomic data. *Cell Syst*. 2019;8(4):281–291.e9.
35 Korsunsky I, Millard N, Fan J, et al. Fast, sensitive and accurate integration of single-cell data with Harmony. *Nat Methods*. 2019;16(12):1289–1296.
36 Yu G, Wang LG, Han Y, He QY. clusterProfiler: an R package for comparing biological themes among gene clusters. *Omics*. 2012;16(5):284–287.
37 Tang F, Li J, Qi L, et al. A pan-cancer single-cell panorama of human natural killer cells. *Cell*. 2023;186(19):4235–4251.e20.
38 Russell AB, Trapnell C, Bloom JD. Extreme heterogeneity of influenza virus infection in single cells. *Elife*. 2018;7.
39 McGinnis CS, Murrow LM, Gartner ZJ. DoubletFinder: doublet detection in single-cell RNA sequencing data using artificial nearest neighbors. *Cell Syst*. 2019;8(4):329–337.e4.
40 Rayes J, Lax S, Wichaiyo S, et al. The podoplanin-CLEC-2 axis inhibits inflammation in sepsis. *Nat Commun*. 2017;8(1):2239.
41 Hinderlich S, Stäsche R, Zeitler R, Reutter W. A bifunctional enzyme catalyzes the first two steps in N-acetylneuraminic acid biosynthesis of rat liver. Purification and characterization of UDP-N-acetylglucosamine 2-epimerase/N-acetylmannosamine kinase. *J Biol Chem*. 1997;272(39):24313–24318.
42 Stäsche R, Hinderlich S, Weise C, et al. A bifunctional enzyme catalyzes the first two steps in N-acetylneuraminic acid biosynthesis of rat liver. Molecular cloning and functional expression of UDP-N-acetyl-glucosamine 2-epimerase/N-acetylmannosamine kinase. *J Biol Chem*. 1997;272(39):24319–24324.
43 Yao L, Korteweg C, Hsueh W, Gu J. Avian influenza receptor expression in H5N1-infected and noninfected human tissues. *FASEB J*. 2008;22(3):733–740.
44 Peng J, Yu L, Huang L, et al. Hepatic sialic acid synthesis modulates glucose homeostasis in both liver and skeletal muscle. *Mol Metab*. 2023;78:101812.
45 Kamiki H, Murakami S, Nishikaze T, et al. Influenza A virus agnostic receptor tropism revealed using a novel biological system with terminal sialic acid knockout cells. *J Virol*. 2022;96(15):e0041622.
46 Bankey P, Prager M, Geldon D, Taylor S, McIntyre K. Acute-phase hepatocytes regulate liver sinusoidal cell mediator production. *Arch Surg*. 1994;129(11):1166–1171.
47 Choby JE, Skaar EP. Heme synthesis and acquisition in bacterial pathogens. *J Mol Biol*. 2016;428(17):3408–3428.
48 Lv C, Huang L. Xenobiotic receptors in mediating the effect of sepsis on drug metabolism. *Acta Pharm Sin B*. 2020;10(1):33–41.
49 Rao RK, Samak G. Bile duct epithelial tight junctions and barrier function. *Tissue Barriers*. 2013;1(4):e25718.
50 Yamada S, Ueguchi T, Mihara N, Matsuzawa H, Sukenobu Y, Komizu M. [Observer performance of PACS-oriented digitized mammography in the detection of fibrils, microcalcifications, and masses: a phantom study]. *Nihon Hoshasen Gijutsu Gakkai Zasshi*. 2009;65(5):620–625.
51 Naficy K. Human influenza infection with proved viremia. Report of a case. *N Engl J Med*. 1963;269:964–966.
52 Roberts GT, Roberts JT. Postsplenectomy sepsis due to influenzal viremia and pneumococcemia. *Can Med Assoc J*. 1976;115(5):435–437.
53 Wu XX, Zhao LZ, Tang SJ, et al. Novel pathogenic characteristics of highly pathogenic avian influenza virus H7N9: viraemia and extrapulmonary infection. *Emerg Microbes Infect*. 2020;9(1):962–975.
54 Zhang S, Hu B, Xu J, Ren Q, Wang L, Wang S. Influenza A virus infection induces liver injury in mice. *Microb Pathog*. 2019;137:103736.
55 Likos AM, Kelvin DJ, Cameron CM, Rowe T, Kuehnert MJ, Norris PJ. Influenza viremia and the potential for blood-borne transmission. *Transfusion*. 2007;47(6):1080–1088.
56 Ru YX, Li YC, Zhao Y, et al. Multiple organ invasion by viruses: pathological characteristics in three fatal cases of the 2009 pandemic influenza A/H1N1. *Ultrastruct Pathol*. 2011;35(4):155–161.
57 Carmona F, Carlotti AP, Ramalho LN, Costa RS, Ramalho FS. Evidence of renal infection in fatal cases of 2009 pandemic influenza A (H1N1). *Am J Clin Pathol*. 2011;136(3):416–423.
58 Pan HY, Yamada H, Chida J, et al. Up-regulation of ectopic trypsins in the myocardium by influenza A virus infection triggers acute myocarditis. *Cardiovasc Res*. 2011;89(3):595–603.
59 Ni Z, Wang J, Yu X, et al. Influenza virus uses mGluR2 as an endocytic receptor to enter cells. *Nat Microbiol*. 2024;9(7):1764–1777.
60 Davis LE, Kornfeld M, Daniels RS, Skehel JJ. Experimental influenza causes a non-permissive viral infection of brain, liver and muscle. *J Neurovirol*. 2000;6(6):529–536.
61 Filgueiras-Rama D, Vasilijevic J, Jalife J, et al. Human influenza A virus causes myocardial and cardiac-specific conduction system infections associated with early inflammation and premature death. *Cardiovasc Res*. 2021;117(3):876–889.
62 Zheng M, Karki R, Vogel P, Kanneganti TD. Caspase-6 is a key regulator of innate immunity, inflammasome activation, and host defense. *Cell*. 2020;181(3):674–687.e13.
63 Yu J, Li H, Jia J, et al. Pandemic influenza A (H1N1) virus causes abortive infection of primary human T cells. *Emerg Microbes Infect*. 2022;11(1):1191–1204.
64 Cao M, Wang G, Xie J. Immune dysregulation in sepsis: experiences, lessons and perspectives. *Cell Death Discov*. 2023;9(1):465.
65 Delorey TM, Ziegler CGK, Heimberg G, et al. COVID-19 tissue atlases reveal SARS-CoV-2 pathology and cellular targets. *Nature*. 2021;595(7865):107–113.
66 Bräuninger H, Stoffers B, Fitzek ADE, et al. Cardiac SARS-CoV-2 infection is associated with pro-inflammatory transcriptomic alterations within the heart. *Cardiovasc Res*. 2022;118(2):542–555.
67 Hinze C, Kocks C, Leiz J, et al. Single-cell transcriptomics reveals common epithelial response patterns in human acute kidney injury. *Genome Med*. 2022;14(1):103.
68 Quarleri J, Delpino MV. Molecular mechanisms underlying SARS-CoV-2 hepatotropism and liver damage. *World J Hepatol*. 2024;16(1):1–11.